Executive Summary of Accomplishments

Our research project entitled *"Electronic Properties and Device Applications of III-V Compound Semiconductor Native Oxides"* was focused primarily on developing and understanding InAlP wet thermal native oxides for GaAs-based electronic devices and yielded the following notable results:

• First demonstration of microwave-frequency operation of a GaAs metal-oxide-semiconductor field-effect transistor (MOSFET) fabricated using wet thermal oxidization of InAlP lattice-matched to GaAs to form a native oxide gate insulator. For 1-μm gate length devices, a cutoff frequency (f_t) of 13.7 GHz and a maximum frequency of oscillation (f_{max}) of 37.6 GHz were obtained [1].

• Follow-on use -- Technology Assist: Notre Dame has negotiated a collaborative research agreement with RF Micro Devices, Inc. (Greensboro, NC) to investigate potential of III-V compound semiconductor native oxides for commercial GaAs-based MOSFET devices.

• First demonstration of scalability of InAlP to thinner (~10-20 nm) films more suitable for devices, maintaining excellent insulating and unpinned interface properties. Extremely low leakage current densities observed even for these device-thickness films, with values comparable and often lower than that of other candidate GaAs gate dielectrics [2].

• First reported III-V metal-oxide-semiconductor field-effect transistor (MOSFET) device utilizing native oxide of InAlP as the gate insulator [3].

• Observation via Transmission Electron Microscopy (TEM) imaging that interfacial precipitates, which decrease in size with decreasing oxidation time, are completely absent in ~20 nm thick oxide films. Identification of precipitates as In rich [2, 6].

• Development of new variable-temperature impedance spectroscopy measurement technique to determine low total interface state density of D_{it}= 8 x 10^{11} cm^{-2} for a 110 nm thick InAlP native oxide film. Trap activation energies were found (E_a=0.17 eV from bias-dependent impedance spectra, 0.40 eV from measurements of temperature-dependent impedance spectra [4, 7].

• Identification via transmission electron microscopy analysis in diffusion marker experiment of inward growth of InAlP native oxide, key to achieving electrically clean oxide/semiconductor interfaces [5].

• Determination of InAlP native oxide bandgap (≥ 4.0 eV) and optical constants [2, 6].

• Determination of mass density of InAlP native oxide films via X-ray reflectivity measurements.

REPORT DOCUMENTATION PAGE

Form Approved
OMB No. 0704-0188

PLEASE DO NOT RETURN YOUR FORM TO THE ABOVE ORGANIZATION.

1. REPORT DATE *(DD-MM-YYYY)*	2. REPORT TYPE	3. DATES COVERED *(From - To)*
02-03-2006	Final Technical	01-05-2001 to 30-04-2005

4. TITLE AND SUBTITLE

Electronic Properties and Device Applications of
III-V Compound Semiconductor Native Oxides

5a. CONTRACT NUMBER

5b. GRANT NUMBER

AF-F49620-01-1-0331

5c. PROGRAM ELEMENT NUMBER

6. AUTHOR(S)

Profs. Douglas C. Hall*, Patrick J. Fay*, Thomas H. Kosel* and
Bruce A. Bunker†: Departments of *Electrical Engineering and †Physics,
University of Notre Dame du Lac

and Subcontractor Prof. Russell D. Dupuis, Georgia Institute of Technology

5d. PROJECT NUMBER

5e. TASK NUMBER

5f. WORK UNIT NUMBER

7. PERFORMING ORGANIZATION NAME(S) AND ADDRESS(ES)

The University of Notre Dame, Department of Electrical Engineering,
Notre Dame, IN 46556-5637
and Georgia Institute of Technology, School of Electrical and Computer Engineering,
777 Atlantic Drive NW, Atlanta GA 30332-0250

8. PERFORMING ORGANIZATION REPORT NUMBER

9. SPONSORING/MONITORING AGENCY NAME(S) AND ADDRESS(ES)

Air Force Office of Scientific Research
ATTN: Dr. Gerald L. Witt - NE
Program Manager, Physics & Electronics
875 North Randolph Street, Suite 325, Room 3112
Arlington, VA 22203-1768

10. SPONSOR/MONITOR'S ACRONYM(S)

AFOSR

11. SPONSOR/MONITOR'S REPORT NUMBER(S)

AFRL-SR-AR-TR-06-0148

12. DISTRIBUTION/AVAILABILITY STATEMENT

Approved for Public Release; Distribution Unlimited

13. SUPPLEMENTARY NOTES

14. ABSTRACT

Notre Dame has demonstrated the first gallium arsenide (GaAs)-based metal-oxide-semiconductor field-effect-transistor (MOSFET) utilizing a native oxide gate dielectric which has excellent microwave frequency performance and, due to its low gate leakage, promises both low-power operation and potential for superior power amplifier devices. We have shown that the wet-thermal native oxides of the compound semiconductor indium aluminum phosphide (InAlP) can be scaled to thicknesses required for devices (10-20 nm) and still maintain their excellent electrical insulating properties and electrically-clean interfaces, making them well-suited for MOS electronic devices. Applications include reduced power consumption, enhanced performance electronic devices (both low-power and high-power amplifiers) to extend battery life of portable or remotely-powered wireless communications equipment, of great potential interest to the military.

15. SUBJECT TERMS

GaAs Metal-Oxide-Semiconductor Field-Effect Transistor (MOSFET), InAlP native oxides, MOS electronic devices

16. SECURITY CLASSIFICATION OF:			17. LIMITATION OF ABSTRACT	18. NUMBER OF PAGES	19a. NAME OF RESPONSIBLE PERSON
a. REPORT	b. ABSTRACT	c. THIS PAGE			Prof. Douglas C. Hall, Ph.D.
U	U	U	UU		19b. TELEPHONE NUMBER *(Include area code)* (574) 631-8631

Publications

[1] Y. Cao, X. Li, P. Fay, J. Zhang, T. H. Kosel and D. C. Hall, "Microwave Performance of GaAs MOSFET with Wet-Thermally-Oxidized InAlP Gate Dielectric," accepted for publication in IEEE Electron Device Letters, in press (May 2006).

[2] Y. Cao, J. Zhang, X. Li, T. H. Kosel, P. Fay, and D. C. Hall, X. Zhang, R. D. Dupuis, J. B. Jasinski and Z. Liliental-Weber, "Electrical properties of InAlP native oxides for metal-oxide-semiconductor device applications," Applied Physics Letters, vol. 86, article 062105 (February 7, 2005).

[3] X. Li, Y. Cao, D. C. Hall, P. Fay, B. Han, A. Wibowo and N. Pan, "GaAs MOSFET Using InAlP Native Oxide as Gate Dielectric," IEEE Electron Device Letters, vol. 25, pp. 772-774 (2004).

[4] Xiang Li, Y. Cao, D. C. Hall, P. Fay, X. Zhang and R. D. Dupuis, "Electrical characterization of native-oxide InAlP/GaAs metal-oxide-semiconductor heterostuctures using impedance spectroscopy," Journal of Applied Physics, vol. 95, pp. 4209-4212 (2004).

[5] J. Xhang, Y. Cao, T.H. Kosel, R.E Cook, and D.C. Hall, "A TEM Study of Wet Oxidation of InAlP on GaAs, submitted to *Microscopy & Microanalysis 2006,* Annual Meeting of the Microscopy Society of America and the Microbeam Analysis Society (Chicago, Illinois, July 30-August 3, 2006).

[6] Y. Cao, J. Zhang, X. Li, T. H. Kosel, P. Fay, D. C. Hall, R. E. Cook, X. Zhang, and R. D. Dupuis, "Electrical Properties and Microstructure of InAlP Native Oxides for MOS Applications," *46th Electronic Materials Conference,* paper GG3 (Notre Dame, Indiana, June 23-25, 2004).

[7] X. Liang, Y. Cao, D. C. Hall, P. Fay, X. Zhang, and R. D. Dupuis, "InAlP Native Oxide/GaAs MOS Heterostructure Interface State Density Measured by Impedance Spectroscopy," *46th Electronic Materials Conference*, paper GG4 (Notre Dame, Indiana, June 23-25, 2004).

[8] T. H. Kosel, D. C. Hall, R. D. Dupuis, R. D. Heller and R. E. Cook, "CuPt-Type Ordering of MOCVD $In_{0.49}Al_{0.51}P$," *Proc. Microscopy and Microanalysis 2002*, Microscopy Society of America (Quebec City, Canada, Aug. 4-8, 2002).

[9] P. J. Barrios, D. C. Hall, U. Chowdhury, R. D. Dupuis, J. B. Jasinski, Z. Lilental-Weber, T. H. Kosel, and G. L. Snider, "Properties of InAlP Native Oxides Supporting MOS Inversion-layer Behavior," *43rd Electronic Materials Conference* (Notre Dame, IN, June 2001).

Dissertations

Xiang Li, "Electrical Properties and Device Applications of InAlP Native Oxide/GaAs MOS Structures", Ph.D. dissertation, June 2005 (Advisor: Prof. Patrick Fay).
Available electronically from http://www.ProQuest.com/products_umi/dissertations/

Ying Cao, "Investigation of InAlP Native Oxides for Metal-Oxide-Semiconductor Device Applications" Ph.D. dissertation proposal, approved August 2005; Final defense expected August 2006. (Advisor: Prof. Douglas C. Hall).

Jing Zhang, Ph.D. dissertation proposal on correlation between microstructure of InAlP oxide/GaAs films and interfaces and GaAs MOS device electrical performance, to be defended Summer 2006.

Cumulative List of Personnel

Faculty:

Prof. Douglas C. Hall, PI
Prof. Patrick J. Fay
Prof. Gregory L. Snider
Prof. Thomas H. Kosel
Prof. Bruce A. Bunker

Graduate Research Assistants:

Xiang Li (full support; advisor: Fay)
Rajkumar Sankaralingam (1/2 month support only; advisor: Fay)
Aaron Stuckey (half-time support; advisor: Bunker)
Bhoophesh Mishra and Seong-Kyun Cheong (partial support; advisor: Bunker)
Ying Cao (full support; advisor: Hall)
Nathan Crain and Prakash Potukuchi (partial support; advisor: Hall)
Jing Zhang (full support; advisor: Kosel)
Ling Zhou (9 months - department support only; advisor: Kosel)

Appendices

The following internal reports and other documents, not readily available elsewhere, are attached here for completeness:

A. Report from Prof. Thomas H. Kosel (TEM characterization results)
B. Report from Prof. Bruce Bunker (X-ray characterization results)
C. Report from subcontractor Prof. Russell D. Dupuis (Crystal growth results)
D. Ying Cao Candidacy Proposal (unpublished, August 2005)

TEM Studies of InAlP Native Oxide

Prof. Thomas H. Kosel, University of Notre Dame

The Dark Particle Layer

Dark particles approximately 10 nm in diameter were observed by TEM at the bottom of the oxide layer (i.e. near the oxide-semiconductor interface) in earlier studies of wet oxidation of InAlP [1, 2]. These particles were thought to be the cause of increased leakage current when the oxide thickness was reduced by etching [3], and could also have other undesirable effects due to non-uniformity of the oxide. As proposed, we have therefore undertaken TEM studies of the oxide to determine the effects of oxidation conditions (temperature, time and oxidation atmosphere) and starting material.

The composition of the dark particles was initially suspected to be In-rich. Evidence supporting this includes the fact that the particles appear dark in bright-field (BF) TEM and BF STEM images, but are white in Z-contrast STEM images, which are lighter in regions of higher average atomic number (Z) [9/03 annual report]. We also reported [9/03 annual report] that one hour of 500 °C dry oxidation following complete 500°C wet oxidation eliminated the dark particles, but produced In diffusion into the GaAs substrate, as evidenced by Z-contrast STEM images showing an irregular white layer, and EDXS spectral identification of In in the diffused layer. This is consistent with the assumption that the dark particles (which were initially present after wet oxidation) are In-rich, since they disappeared during the dry oxidation step. In addition, Graham et al. [4] used Auger depth profiling to characterize InAlP wet oxidized at 500 °C, and identified a significant In peak in a thin layer very near the oxide/semiconductor interface. This is perhaps the best evidence that the particles are In-rich. However, it should be noted that Graham et al. [4] included TEM evidence that the layer of dark particles had disappeared without forming an observable layer of In diffusion into the GaAs. This reason for this disagreement is unclear, since we both used the same wet oxidation temperature, although we used one hour for both wet and dry oxidation steps, whereas they used half an hour.

Direct EDXS determination of the composition of the dark particles has been severely hampered by the extreme sensitivity of the oxide to electron beam damage in the TEM, as we discussed earlier [9/03 annual report]. It was hoped that our upgrade of our TEM to include EDXS and STEM might permit direct proof that the particles are In-rich by x-ray mapping, if rapid scanning many frames would avoid beam damage by heating. (Rescanning the same area multiple times during x-ray mapping is not possible with the Tecnai 20 STEM system which we have used at Argonne National Laboratory, due to software limitations.) However, electron beam damage still occurs during rapid multiple-frame x-ray mapping with our new Thermo-Noran EDXS system, even with small probe currents. Damage occurs well before enough x-ray counts are detected to provide useful statistics for particle identification, in either cross-sectional or plan-view TEM specimens. An example of the damage that occurs in the oxide after leaving a 25 nm beam spot stationary for 3 minutes is included in Fig. 1. The damage consists of a white central region, surrounded by dark particles which we have identified as being In-rich using EDXS.

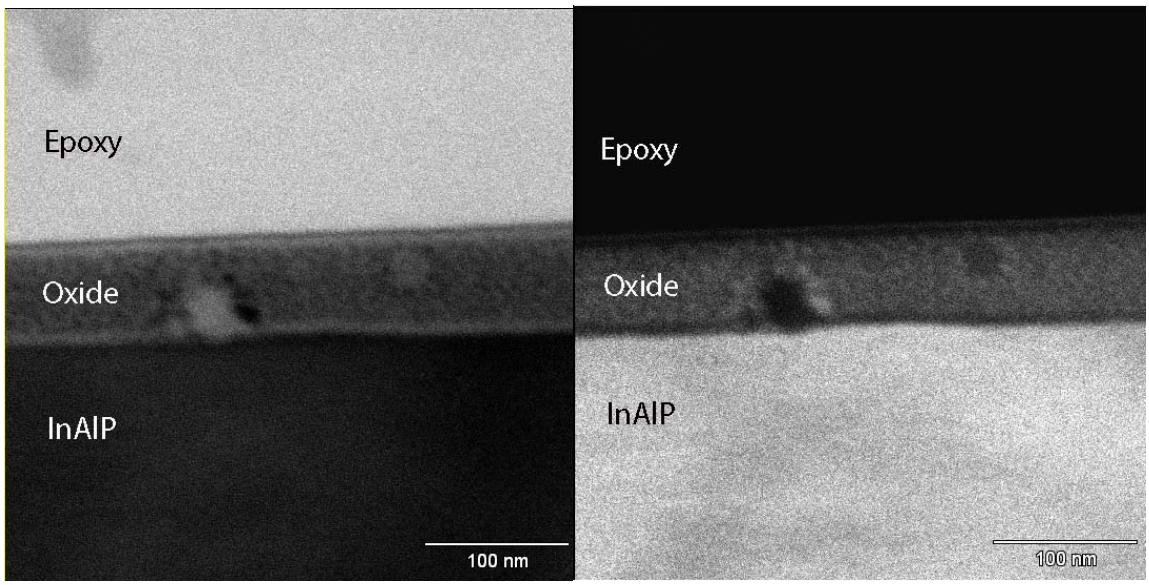

Figure 1. Beam damage in InAlP native oxide

Nevertheless, we were able to obtain some evidence that particles are In-rich using repeated EDXS linescans (in which the beam is moved to successive pixels along a line in the image). Unfortunately, the dwell time at each pixel during linescans is limited by software to a minimum of 0.1 s, but repeated linescans can be done. The first linescan generally produces an identifiable In peak at the position of a dark particle, but the number of counts in a single scan is too small to give unambiguous statistics. As more scans accumulate, the counting statistics improve, but In counts begin to accumulate in regions away from particle, due to beam damage. Fig. 2a shows one of our best linescans, with a clear In peak at the particle location. However, most scans deteriorated after this point, such as Fig. 2b, in which the peak at the particle location ceased increasing after the first scan, and In counts accumulated elsewhere, giving the false appearance of high In concentration in the original oxide at locations away from the dark particles. After only a few scans, the peak at the particle was no longer visible in a given linescan. Nevertheless, taken together with the other evidence, these observations help make it clear that the particles are In-rich.

The particles are apparently also crystalline, since we were able to briefly see lattice fringes in them. Usually they disappeared from the image after too short a time to obtain an image on film, as discussed earlier (9/03 annual report). After many attempts, we obtained the lattice image in Fig. 3, demonstrating the crystalline nature of the particles. Disappearance of the particles in the TEM beam occurs even when the beam is defocused enough to cause no observable damage to the surrounding oxide in cross-sectional TEM specimens. We attributed this (9/03 annual report) to their evaporation into the TEM column vacuum. Ion milling also causes loss of the particles in the thinnest parts of XS specimens, for the same reason. However, we find that in plan-view TEM specimens, the particles remain stable in the TEM beam, since they are isolated from the vacuum by the oxide on one side and the thinned substrate on the other. A TEM image of the particles in a plan-view TEM specimen is shown in Fig. 4.

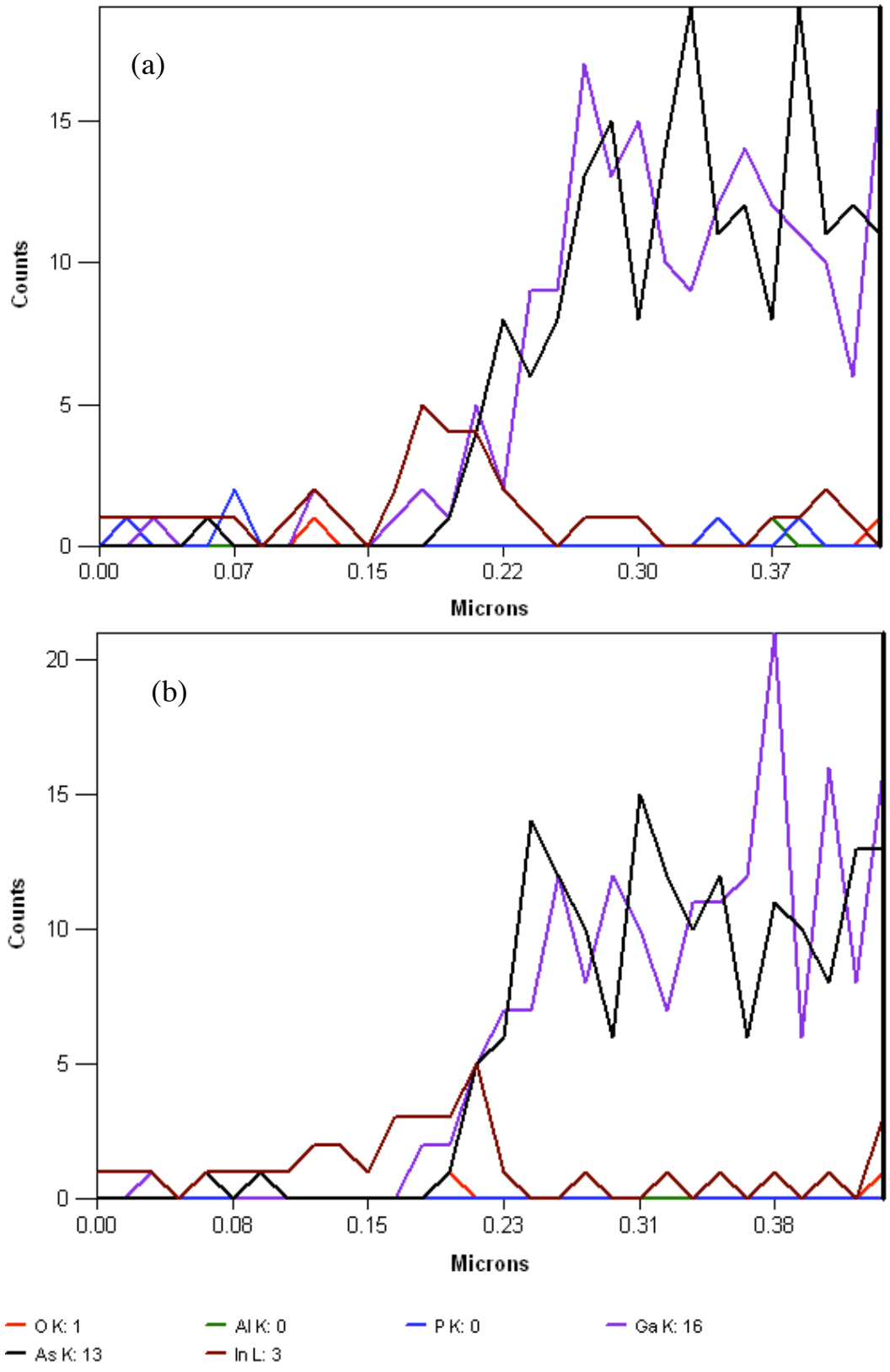

Figure 2. a) Best Energy-dispersive X-ray Spectroscopy (EDXS) line across particle; b) typical linescan

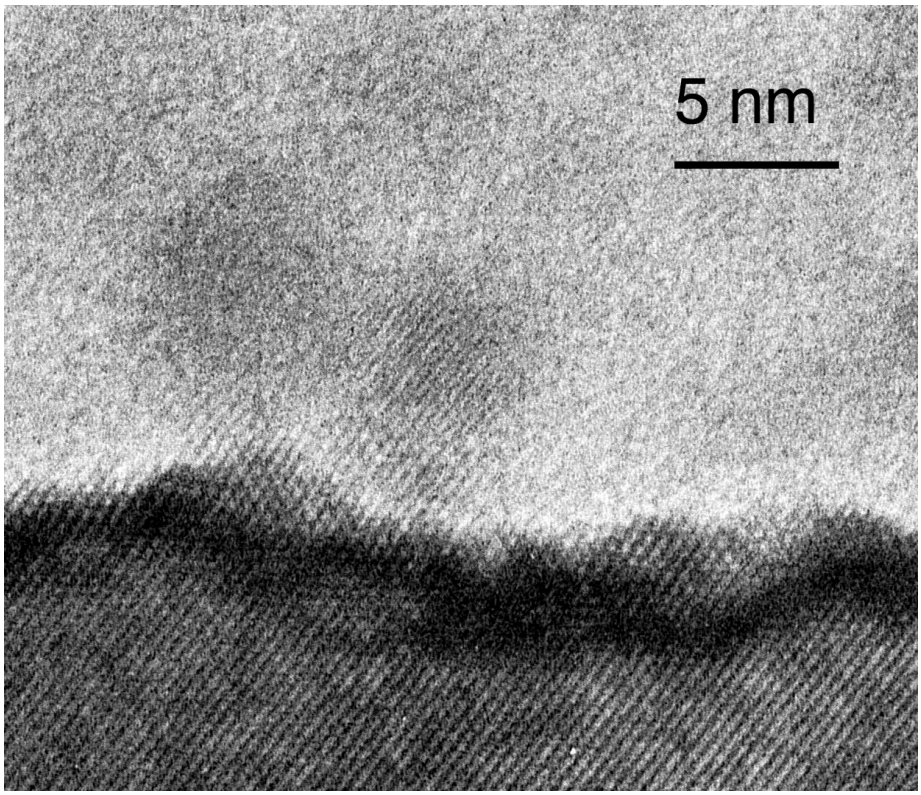

Figure 3. Lattice fringes in dark particle within InAlP native oxide.

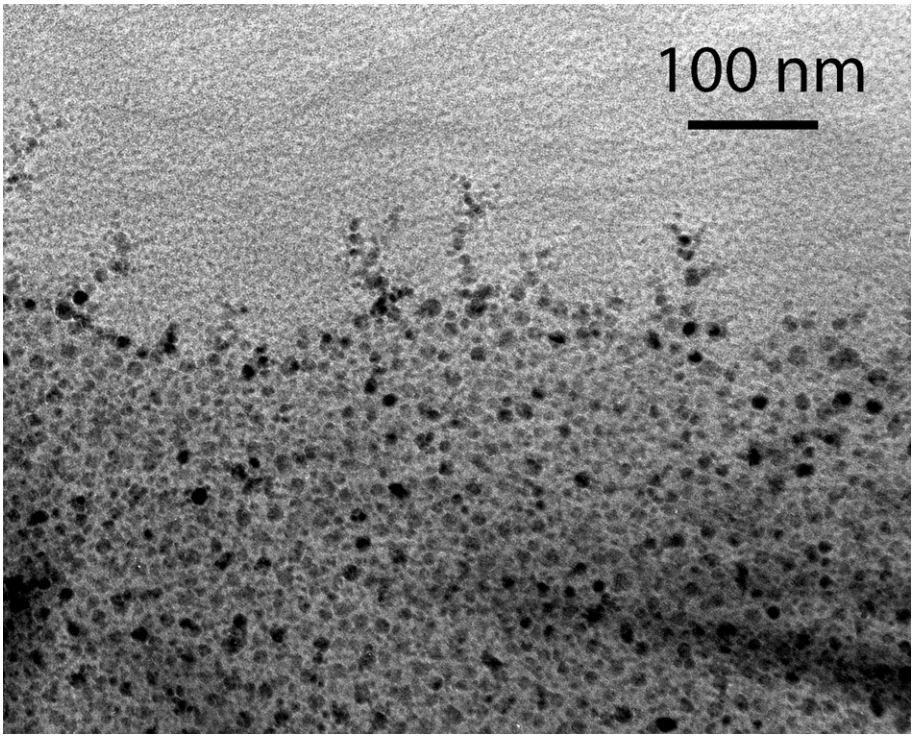

Figure 4. Plan view specimen showing particles.

Because of the overlayer of amorphous oxide, lattice imaging of the particles in PV specimens is not possible. X-ray linescans and maps still do not permit direct confirmation of the In-rich particle composition, due to beam damage in the overlying [oxide. It is possible that the particles are unoxidized metallic In, as suggested by Graham et al. [4], but we cannot confirm this at this time. Future work could attempt to confirm or refute this by comparing the lattice fringe spacing with those of metallic In.

Diffusion Marker Experiment

The In-rich particles were believed to form due to slower diffusion of In to the outer surface of the oxide, where we assumed oxide was forming. This was consistent with our observations [5] that the particle size increased with oxidation time and oxide thickness, and that in a 17 nm oxide formed from a 15 nm InAlP film, no particles were observed in TEM cross-sectional or plan-view specimens.

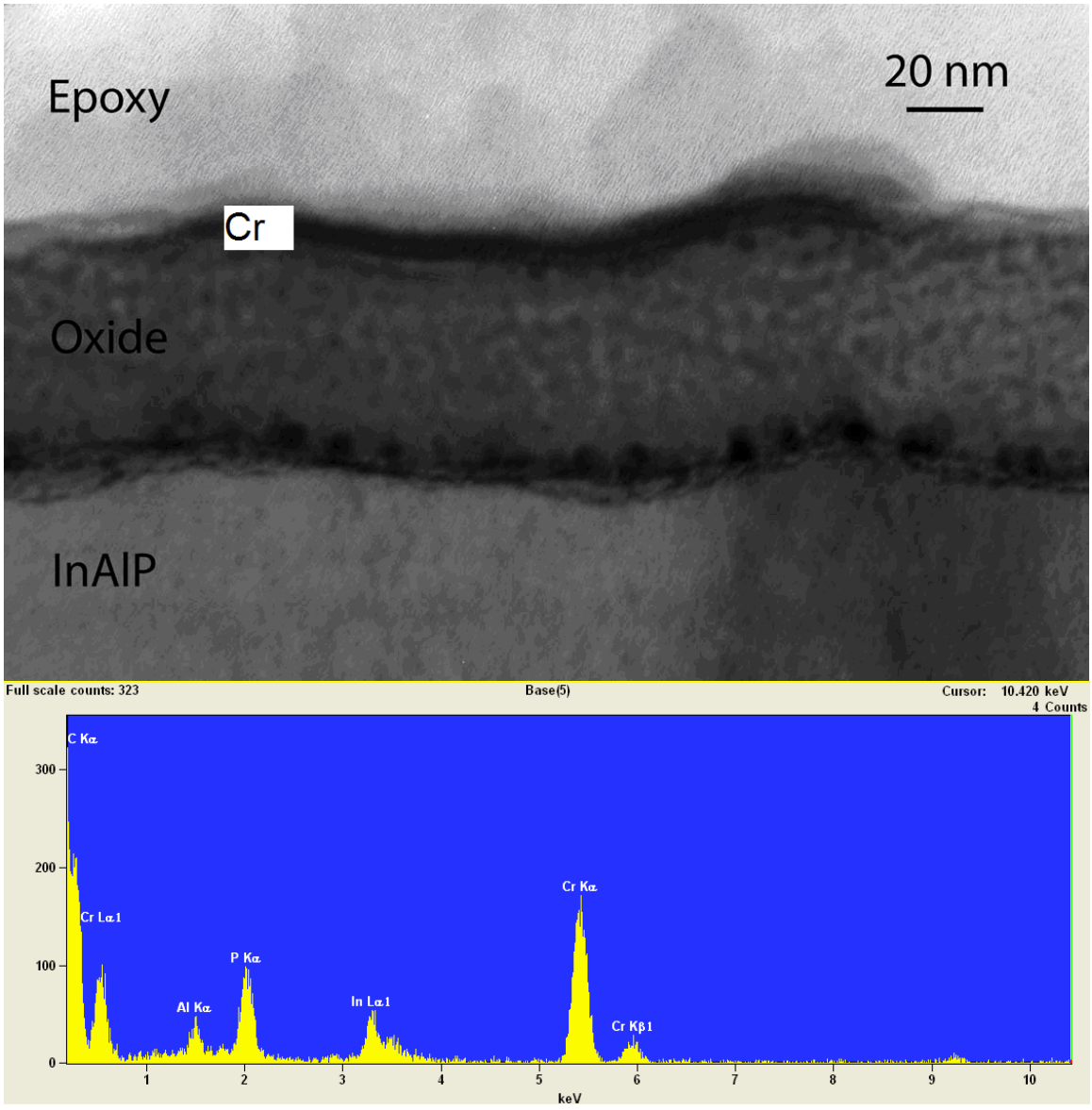

Figure 5. Cr marker TEM image (top) and EDXS spectrum (bottom).

In the original proposal, we planned to use a diffusion marker experiment to determine whether the oxide grows primarily by transport of O (oxygen) to the InAlP/oxide interface, producing new oxide there, or by transport of the semiconductor elements (In, Al and P) to the outer oxide surface, producing new oxide there. In our 9/04 annual report, we showed narrow W (tungsten) lines produced by e-beam lithography on the InAlP surface to act as diffusion markers. If the oxide grows primarily by inward O diffusion, the markers would be found at the outer surface, since new oxide would be formed underneath the markers. Conversely, if oxidation occurs primarily by out-diffusion of the semiconductor elements, the marker particles should be found at the oxide/InAlP interface. The latter case would be consistent with the observation of In particles at the interface. The W marker experiment failed, since we were unable to locate the W after the oxidation, apparently because it diffused into the oxide. However, we did obtain good diffusion marker results using Cr lines produced by e-beam lithography. The Cr lines are 177 nm wide and 4 nm thick with 2 um spacing between lines. Fig. 5 (top) shows a cross-sectional TEM image showing that the Cr was left on the *outer surface* after oxidation. The dark feature labeled Cr was confirmed to be Cr-rich using EDXS (Fig. 5, bottom). We believe the Cr is oxidized, but Cr oxide which does not diffuse into the oxide is still a valid diffusion marker material.

The observation that the Cr markers are observed on the outer surface of the oxide shows that oxidation must proceed primarily by inwards diffusion of O to the oxide/InAlP interface, producing new oxide there. This is encouraging in terms of the oxide properties, since it shows that pre-existing surface impurities will remain on the outer oxide surface, thus not contaminating the interface and causing interface states. However, this result clearly conflicts with our previous assumption that slow out-diffusion of In is responsible for the In-rich particles. One can imagine that the In is less easily oxidized than Al and P, leaving an excess of unoxidized In in the thin layer of oxide grown most recently at the interface, but each new layer should have the same excess In content, leaving the In content of the oxide constant. One can also imagine that In particles nucleate near the interface due to failure to oxidize, but in order to explain the fact that they are always observed near the interface it is then necessary to assume that they travel through the oxide to keep up with the moving interface. While it is well known that particles can move by surface diffusion, the driving force for this motion is not clear. Another possibility is that the particles are not actually formed during oxidation, but only during cooling. Further experiments would be needed to test this theory, but it is attractive since it is common for solubility to decrease with temperature, leading to precipitation of particles. They may nucleate near the interface due to heterogeneous nucleation, although this might be expected to lead to hemispherical rather than the approximately spherical particles observed. Once nucleated, they could grow by depleting In from the overlying oxide. If the particles form by precipitation during cooling, rapid cooling could prevent this. Since the diffusion marker experiment was completed at the very end of this project, we did not had time to reconcile the result with the In-rich particle observations, or to do new experiments to try to further evaluate explanations such as those suggested here.

Improvement of Oxide Uniformity

TEM was useful in confirming the origin of diode-like I-V characteristics observed with the 7 nm wet oxide from a 5 nm InAlP epilayer from our subcontractor (Dupuis). In our EMC presentation [5],[6], we tentatively attributed this to pinholes in this very thin oxide. TEM cross-sections later showed that the oxide was discontinuous (Fig. 6a), while the original epilayer was uniform (Fig. 6b). This caused a re-evaluation of the citric acid concentration and time used for removal of the GaAs capping layer. After adjusting this, the oxide was continuous, of uniform thickness and, consistent with the earlier observations for the thinnest oxides, free of dark particles. The leakage current was decreased by about three orders of magnitude by this improvement of process conditions.

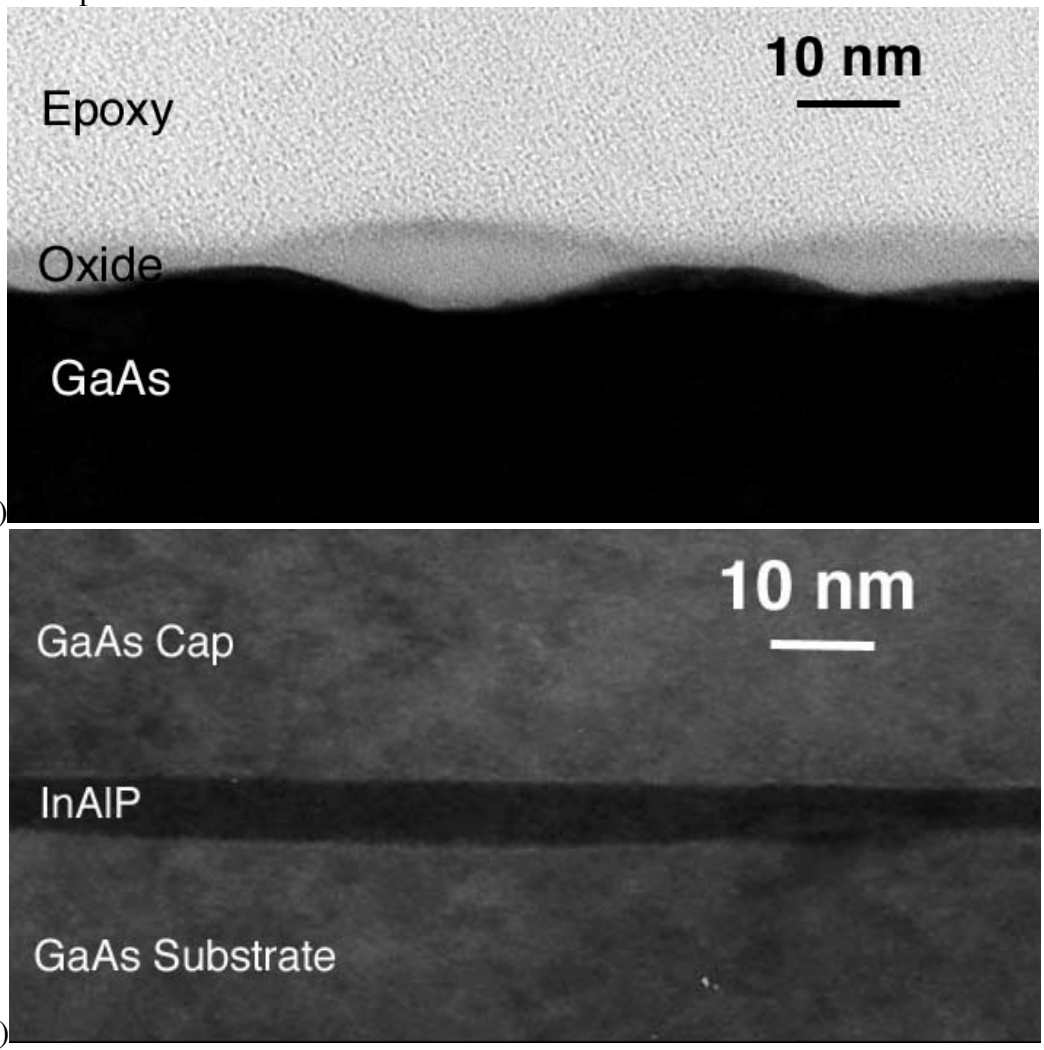

Figure 6 (a) discontinuous oxide; (b) unoxidized 5 nm InAlP. With improved etching, oxide thickness became uniform (not shown).

Particles in Thin Oxide

Late in the project, we observed that In-rich particles are located at the bottom of the oxide even in the case of a very thin 10 nm oxide wet oxidized at 440 °C. This result is inconsistent with our earlier observations that particle size decreases with decreasing oxide thickness, with films

thinner than 17 nm appearing to be particle free [5, 6]. Although most of our early results were obtained from 500 °C wet oxidation, a 420 °C oxidation of a 5 nm epilayer (our wafer #E5459) produced a particle-free oxide. Thus, the fact that the new observation is for 440 °C wet oxidation is probably not the reason for the observation of particles in this thin oxide. The most likely difference is that the thin oxide with observed particles was grown on a different wafer from a different supplier (EpiWorks, Inc.). Although TEM revealed no obvious difference between the structures of the starting epilayers, this and other observations suggest that undetected differences in the starting InAlP epilayer may significantly influence the oxide structure and properties, and that further work is needed to correlate the InAlP epitaxial growth conditions and resulting InAlP oxide quality.

Partial Crystallinity of the Oxide

In addition to the In-rich particles observed near the interface, we also observed [5] that isolated nanocrystals are often observed throughout the oxide thickness by high-resolution TEM, demonstrating that the oxide is not entirely amorphous. The stable forms of the $InPO_4$ and Al_2O_3 phases identified in the oxide by XPS (Graham et al. [4]) are crystalline, so it is not surprising that there is some degree of crystallinity within the oxide. We have not observed any systematic variation of the amount of crystallinity with processing variables.

Dry Oxidation

Since initial studies of dry oxidation of InAlP indicated that it formed a very thin oxide with self-limiting thickness and promising electrical properties, a TEM study was undertaken to characterize the structure and thickness of the dry oxide as a function of oxidation temperature. While initial observations showed that a dry oxide had lower leakage current than a wet oxide of the same thickness, further work showed that this was not consistently true. Dry oxidation produced much greater variations in electrical properties than wet oxidation. These variations were attributed to variations in oxide and particle layer thicknesses within a given specimen. Although the self-limiting nature of the dry oxide is attractive from a processing standpoint, the variability of electrical properties led us to end this particular avenue of exploration.

In almost all cases, it was observed that dry oxidation produced a thin amorphous oxide layer, with a thin, crystalline In-rich outer layer that appears dark in bright-field TEM images. The thicknesses of the oxide and dark In-rich layers were measured, and the results are summarized here in Table 1.

Increasing the dry oxidation time from 10 to 60 minutes produced little change in oxide or total thickness at 440 °C, and at 500 °C,180 minutes produced only about 30% greater oxide thickness than 10 minutes. Dry oxidation at 560°C produce a somewhat rough interface, and at 620°C an extremely rough interface (not shown). The table entry for oxide thickness at 620°C represents the maximum and minimum thicknesses of the scalloped interface. Dry oxidation thus produces an essentially self-limiting oxide thickness, which may be due to parabolic diffusion-controlled growth which could be observed for shorter times. Oxide thickness increased with oxidation temperature for 10-minute oxidation times. Fig. 7 shows a high-resolution TEM image of a cross section of the oxide formed after 10 minutes at 440 °C. Lattice fringes are readily visible in the dark outer layer. In this and all other cases, the dark layer consisted of discrete individual particles; in some cases there were gaps between particles.

Table 1. Summary of TEM dry oxidation results

T (°C)	Wafer number	Time (min)	Dark Layer	Oxide thickness (nm)	Dark layer thickness (nm)
380	E5674	10	Top	2.7	2.3
440	E5674	10	Top	4.7	2.7
"	E5674	60	Top	3.6	3.5
"	3-152	10	None	5.1	--
500	E5674	10	Top	9.2	4.8
"	E5674	180	Top	12.1	4.7
"	E4793	10	Top	11.6	5.0
560	E5674	10	Middle	21.4	6.6
620	E5674	10	Top	12.2/3.7	6.2

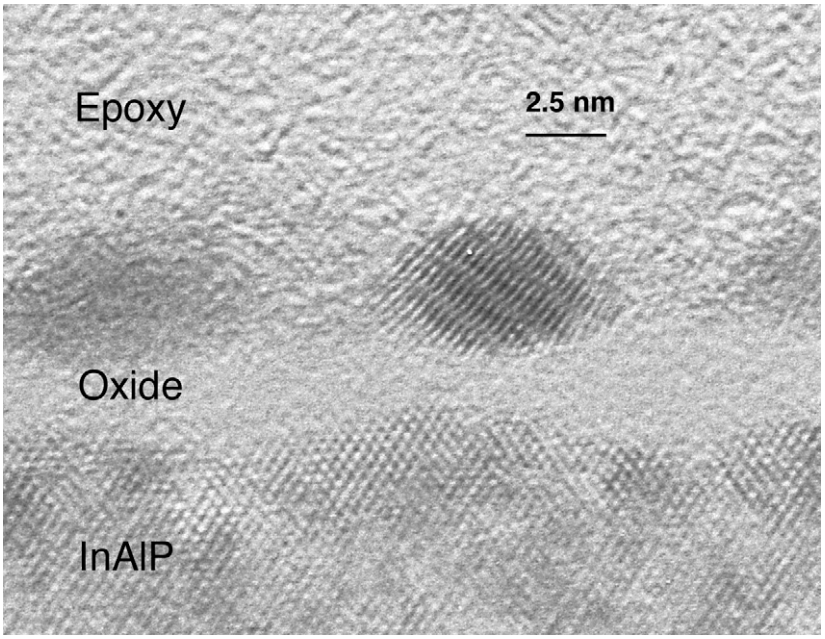

Figure 7. High-resolution TEM image of InAlP film oxidized in dry O_2 at 440°C for 10 min.

Fig. 8 is a bright-field TEM image of the oxide formed by 10 minutes of dry oxidation of our wafer #E5674 at 500 °C, showing that the apparently continuous layer consists of individual particles. This dark layer was much more stable in the electron beam than the dark particles near the interface in wet-oxidized specimens, making it possible to obtain lattice images and EDXS spectra. EDXS shows that the dark layer is clearly In-rich. The dark layer was only absent in one case, and when present was at the top (outer) oxide surface in all cases except one (560 °C). The cause of the dark outer layer could be inward diffusion of O combined with slow oxidation kinetics for In. However, this is not observed for wet oxidation, in which the diffusion marker experiment has demonstrated that oxidation proceeds by inward diffusion of O. The reason for formation of the dark outer layer in dry oxidation is thus not clear at the time of this report.

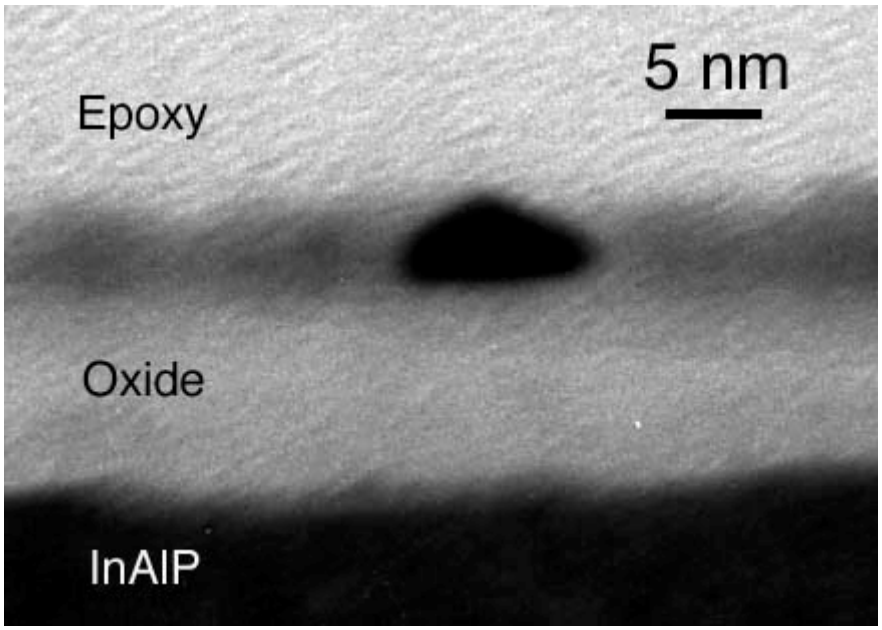

Figure 8. Bright-field TEM image of InAlP film oxidized in dry O_2 at 500 °C for 10 min.

High-Temperature Wet Oxidation

Pulver et al. studied wet oxidation of InAlP at 500 °C, 560°C and 625°C using XPS depth profiling [7]. They observed that at 625 °C, the oxide had an In-depleted layer closer to the interface, resulting in a lower In XPS intensity in the depth profile, and a lighter region in a TEM cross-section of the oxide. Since high-temperature oxidation was thought to potentially provide a means to reduce or eliminate the layer of In-rich particles, we oxidized a specimen at 625 °C. However, the TEM cross-section revealed no evidence of an In-depleted layer near the interface, as shown in Fig. 9. The high temperature oxidized specimen has an undesirably rough interface between the oxidized and unoxidized InAlP, like that observed with dry oxides.

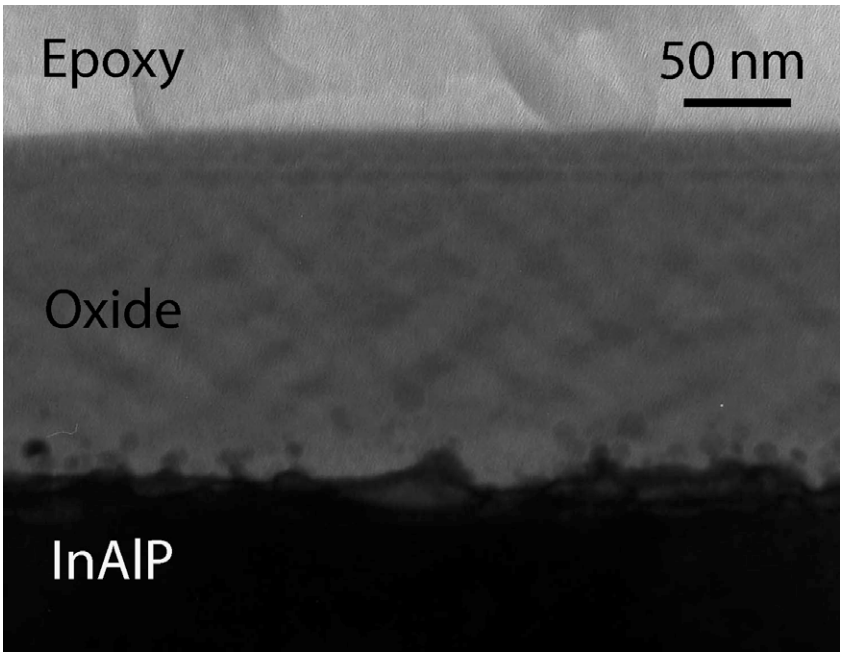

Figure 9. TEM cross section of InAlP oxide grown at 625 °C.

References for TEM report

[1] P. J. Barrios, D. C. Hall, G. L. Snider, T. H. Kosel, U. Chowdhury, and R. D. Dupuis, "Electrical Properties of InAlP Native Oxides For GaAs-Based MOS Applications," in *State-of-the-Art Program on Compound Semiconductors (SOTAPOCS XXXIV), Electrochem. Soc. Proc.*, vol. 2001-1, 2001, pp. 258-264.

[2] D. T. Mathes, R. Hull, R. D. Dupuis, R. D. Heller, and B. P. Tinkham, "Nanoscale structure and chemistry of $Al_{0.49}In_{0.51}P$ thermal oxide," *Applied Physics Letters*, vol. 75, pp. 2572-2574, 1999.

[3] P. J. Barrios, D. C. Hall, U. Chowdhury, R. D. Dupuis, J. B. Jasinski, Z. Lilental-Weber, T. H. Kosel, and G. L. Snider, "Properties of InAlP Native Oxides Supporting MOS Inversion-layer Behavior," presented at 43rd Electronic Materials Conference, Notre Dame, IN, 2001.

[4] M. J. Graham, S. Moisa, G. I. Sproule, X. Wu, J. W. Fraser, P. J. Barrios, D. Landheer, A. J. SpringThorpe, and M. Extavour, "Thermal oxidation of InAlP," *Materials at High Temperatures*, vol. 20, pp. 277-280, 2003.

[5] Y. Cao, J. Zhang, X. Li, T. H. Kosel, P. Fay, P. Barrios, D. C. Hall, R. E. Cook, X. Zhang, and R. D. Dupuis, "Electrical properties and microstructure of InAlP native oxides for MOS applications," presented at 46th Electronic Materials Conference, Notre Dame, Indiana, 2004.

[6] Y. Cao, J. Zhang, X. Li, T. H. Kosel, P. Fay, D. C. Hall, X. B. Zhang, R. D. Dupuis, J. B. Jasinski, and Z. Liliental-Weber, "Electrical properties of InAlP native oxides for metal-oxide-semiconductor device applications," *Applied Physics Letters*, vol. 86, 2005.

[7] D. Pulver, C. W. Wilmsen, D. Niles, and R. Kee, "Thermal oxides of In0.5Ga0.5P and In0.5Al0.5P," *Journal of Vacuum Science and Technology B*, vol. 19, pp. 207-214, 2001.

X-ray Reflectivity Studies of InAlP Native Oxide

Prof. Bruce A. Bunker, University of Notre Dame

As a further investigation of interfaces in oxidized InAlP samples, x-ray reflectivity measurements were undertaken. By measuring the intensity of specular-reflected x-rays from a smooth, flat sample, it is possible to determine the sample density as a function of depth in the sample. These results can be used to determine layer thicknesses, interdiffusion, compound formation, and related interfacial properties.

The samples used for this study were similar to those used for device fabrication. Using metalorganic vapor phase epitaxy, the InAlP layer was first grown upon a GaAs substrate with a GaAs cap layer. An oxide film was prepared at Notre Dame by removal the GaAs cap layer and wet oxidation of the InAlP layer. The oxidation process was timed to allow full oxidation of the InAlP layer.

The x-ray reflectivity measurements were made at the Turner X-ray Laboratory at Goshen College, near Notre Dame. Two samples with different oxide thicknesses were used in this study; the growth structures and post-oxidation structures are shown in the below table. Note that during oxidation, the oxide layer increases in thickness by a factor of 1.8 from the initial as-grown thickness.

Growth And Post-Oxidation Structures for InAlP Materials

Name	Description	Growth Structure (Surface First)	Post-Oxide Structure (Surface First)
E4973	Thick Oxide	GaAs 50nm InAlP 63nm GaAs buffer 500nm GaAs Substrate	InAlP Oxide 113nm GaAs buffer 500nm GaAs Substrate
E4979	Thin Oxide	GaAs 50nm InAlP 29nm GaAs buffer 500nm GaAs Substrate	InAlP Oxide 52nm GaAs buffer 500nm GaAs Substrate

The normalized reflectivity data and best fit for E4973 (thick oxide layer) and E4979 (thin oxide layer) are shown in the following figures. The corresponding fit parameters are shown the following tables for each sample.

Fit Parameters for E4973

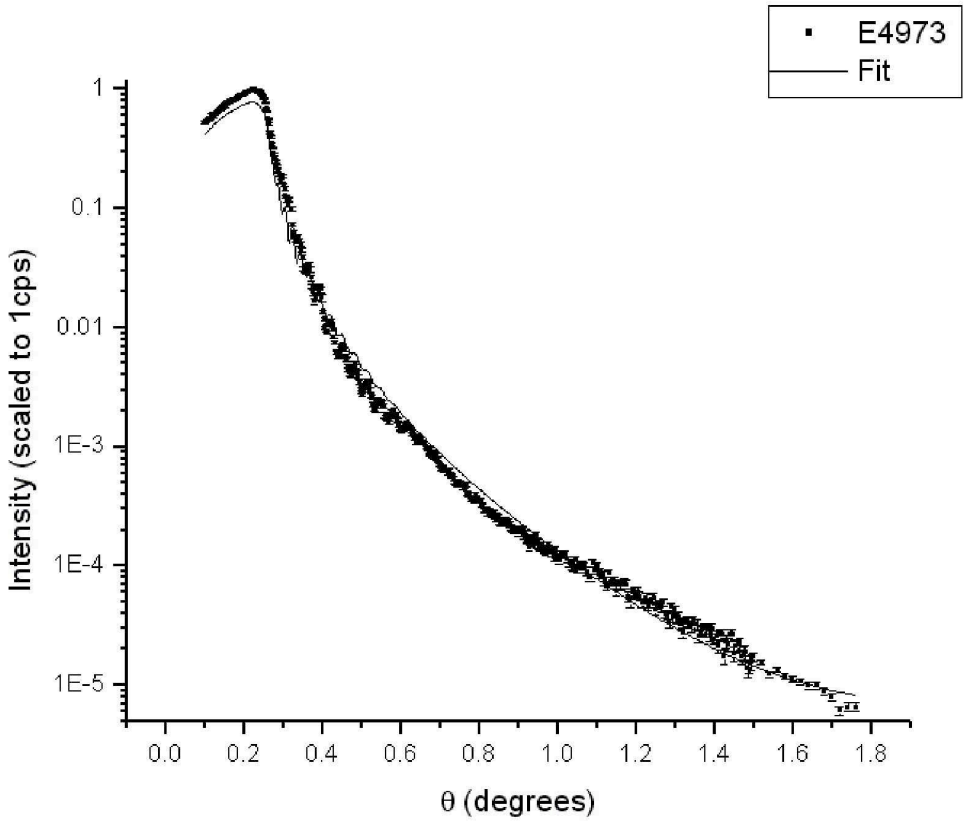

$\chi^2 = 2.1179$				
Type	Thickness	Density	Absorption	Roughness
surface film	5.19±0.01	1.37±0.01	2.68±0.01	1.98±0.01
InAlP Oxide	1087.54±0.01	3.13±0.01	616.94±0.01	10.89±0.01
In Layer	81.41±0.01	4.20±0.01	1199.67±0.01	27.32±0.01
GaAs	100	5.318	5.318	1.98±0.01

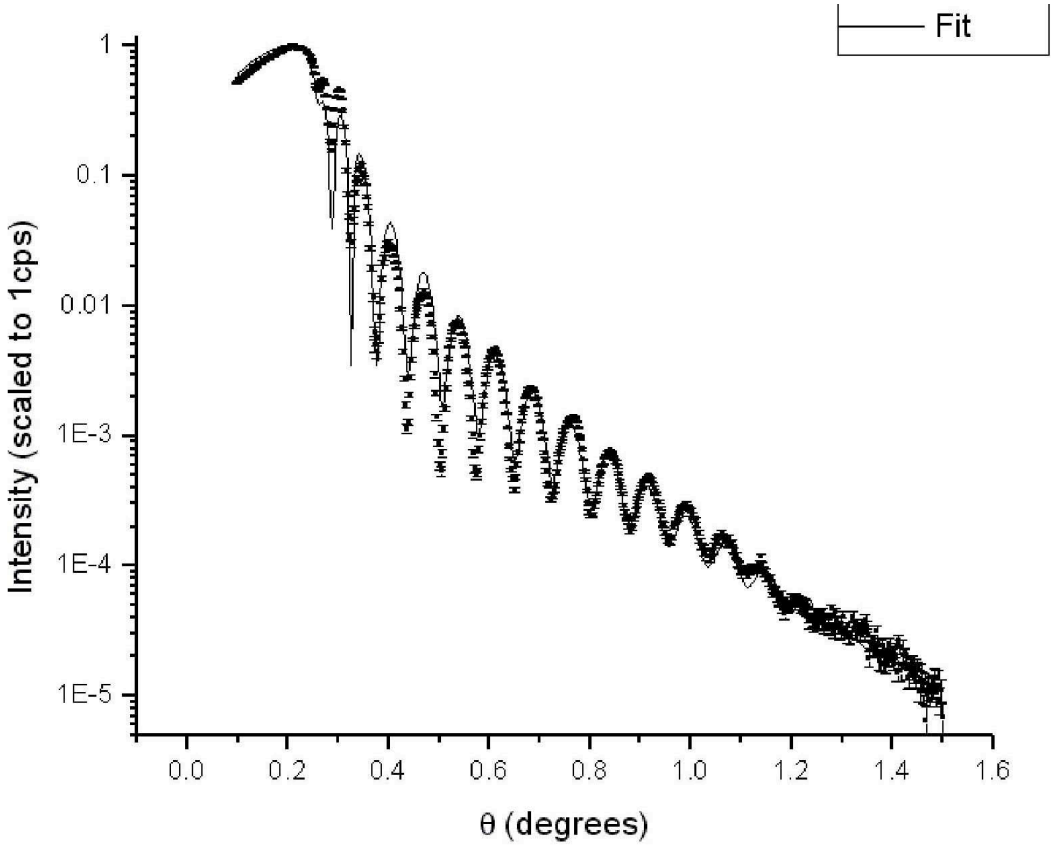

Fit Parameters For E4979

$\chi^2 = 3.0554$				
Type	Thickness	Density	Absorption	Roughness
InAlP Oxide	551.15±0.01	2.95±0.01	967.88±0.01	6.18±0.01
In Layer	32.14±0.01	6.31±0.01	1198.67±0.01	12.72±0.01
GaAs	100	5.318	366.08	15.78±0.01

The x-ray reflectivity from sample E4973 showed two interesting details: a rapid decrease in intensity and high frequency oscillations of small amplitude. Analysis of the reflectivity data showed the rapid decrease in intensity was due to roughness of the surfaces, with a buried layer whose surface roughness was 27 Å. The high frequency, small amplitude oscillations resulted from the thick oxide layer. The oxide layer was found to be 1087.54 Å. thick, which is a factor of 1.73 increase in thickness compared to the original thickness of the film before oxidation. This increase in thickness is similar to results reported elsewhere. Again, as noted earlier, a thin surface film was found. Additionally, a 81Å interface layer was required between the oxide film and the substrate for the best fit to the data. This thin interface film was of higher density and absorption coefficient than the oxide film above it. Based upon the fitting results for the

absorption coe_cient of the thin interface layer it was composed of some form of In or InP. This corroborates TEM results reported elsewhere.[1] Additionally, two possibilities for structure of this layer exist given the thickness of the layer, 81.4Å , and the roughness of the layer, 27.3Å. One possibility is that the interfacial layer is a thin layer with large roughness. The other possibility is that rather than being a true layer, this interfacial layer is a layer of precipitates which form at the top surface of the substrate. In the second possibility, the density of the interface layer would be the average of the density of the precipitates and the material between them, which means that the precipitates could have a higher density than the simulation indicates. However, as the x-ray reflectivity only measures in the z, or depth, direction it is not possible to differentiate the two possibilities based upon the current data.

The x-ray reflectivity from sample E4979 was found to be well-described with 3-layer structure. A surface film did not statistically improve the fit to the data for this material. The surface layer in this case was an oxide film of 551Å. This thickness was a factor of 1.9 increase from the original film, again similar to previously reported results. Below the oxidized film, a thin interfacial layer greatly increased the goodness of fit. The interfacial film again had higher density and absorption coefficient than the oxide layer above it, indicating the presence of a larger percentage of In per unit volume than in the oxide film. The interfacial film again exhibited large surface roughness, approximately one-third of the total interfacial film thickness, which could indicate either a rough layer, or a precipitate layer.

These results show that x-ray reflectivity complement electron microscopy and optical studies, and can be used for a deeper understanding of interfacial properties of these and other semiconductor systems.

---

[1] P. Barrios, D. Hall, G. Snider, T. Kosel, U. Chowdhury, and R. Dupuis, “Electrical properties of InAlP native oxides for GaAs-based MOS applications” in F. Ren, D. Buckley, S. Chu and S. Pearton, editors, Proceedings of the International Symposia: III-Nitride Based Semiconductor Electronics and Optical Devices and Thirty-Fourth State-Of-The-Art Program on Compound Semiconductors (SOTAPOCS XXXIV), The Electrochemical Society Proceedings, pages 258–264, The Electrochemical Society, Pennington, N.J. (2001)

III-V Epitaxial Structures for Native Oxide Studies and Devices

Final Report Submitted by
Prof. Russell D. Dupuis
Georgia Institute of Technology, School of Electrical and Computer Engineering,
777 Atlantic Drive NW, Atlanta GA 30332-0250

Submitted to
Prof. Douglas C. Hall
Notre Dame University, Dept. of Electrical and Computer Engineering,
Notre Dame IN 46556

The InAlP/GaAs and InGaP/InAlP/GaAs samples have been grown on (001) GaAs substrates for MOS and MOSFET device applications. The growths were carried out in an EMCORE GS3200-UTM low-pressure metalorganic chemical vapor deposition (MOCVD) or in a Thomas Swan 7x2 CCS low-pressure MOCVD with a close-coupled showerhead (CCS) system. The sources employed include adduct-purified trimethylindium (TMIn), triethylgallium (TEGa), and trimethylaluminum (TMAl) for Column III elements, and phosphine (PH_3) and arsine (AsH_3) for Column V elements, and Disilane (Si_2H_6) as an n-type dopant. The typical *n*-type MOS structures were grown by initially growing ~ 500nm thick Si doped GaAs with a doping level around n=1e^{17}/cm^3 on a Si doped GaAs substrate followed by growing an ~10-60 nm thick undoped $In_{0.48}Al_{0.52}P$ layer and then a 50 nm thick undoped GaAs layer. The MOSFET structures were grown on semi-insulating GaAs substrates by initially growing a 100 nm thick undoped GaAs, then 100 nm Si doped GaAs with a doping level around 1e^{17}/cm^3, followed by 4 nm thick undoped $In_{0.49}Ga_{0.51}P$ and ~15 nm thick undoped $In_{0.48}Al_{0.52}P$ and finally covered with a 50 nm thick Si-doped GaAs with a doping level of n=6e1e^{18}/cm^3. Before the growth of these structures, the InAlP and the InGaP growth conditions were optimized and their growth rates were calibrated by using X-ray diffraction (XRD) and atomic force microscopy (AFM) in a tapping mode in air at room temperature. XRD measurements were carried out in a four circle, Philips MRD X-ray diffractometer with CuKa as the radiation source. The doping level in GaAs was meassured by electrochemical voltage (ECV) using an Accent PN4300 profiler and also by Hall measurements.

Fig. 1 shows the XRD (004) rocking curves of three InGaP and InAlP single layer samples. The samples were grown at 680 °C with a growth rate around 15 nm/min. The clear observation of pendellosung oscillations and the narrow linewidth of the layer peaks strongly suggest the high quality of the InGaP and InAlP layers. By using a curve fitting process, the composition of the layer can be extracted from the layer peak position; the layer thickness and thus the growth rate are extracted from the period of the oscillation. As an example, the bottom curve is a fitting of the measured curve of sample 3-0386.

The quality and the sharpness of the interface between the III-P alloys and GaAs can be tested by growing III-P/GaAs superlattices (SLs). Fig. 2 shows the XRD (004) ω-2θ scan of an $In_{0.49}Ga_{0.51}P$ (20 nm)/GaAs (20 nm) 10 period SL. Up to ± 20 satellite peaks are seen in the curve. This number is the highest observed so far in InGaP/GaAs SLs, to the best of our knowledge. Usually the linewidth and the number of the satellite peaks are directly related to the sharpness of interface in the SL. The many satellite peaks in the XRD curve indicates that the interface is very sharp in the grown structures. Fig. 3 (a) and (b) shows the surface morphology

of 450 nm thick InAlP with and without 20 nm GaAs cap layer, respectively. We see that monolayer-high atomic steps are clearly seen on caped sample. The surface RMS is around 0.1 nm in images (a) and around 0.4 nm in (b). The slight rougher surface in (b) has a kinetic origin and usually the growth front becomes rough with the layer thickness. We think, for 10-60 nm thick InAlP in the MOS and MOSFET structures, this roughening is negligible, as can be also inferred from the XRD results shows in Fig. 2, where the InGaP layer is 20 nm thick. The device structures were grown at the optimized conditions based on these studies.

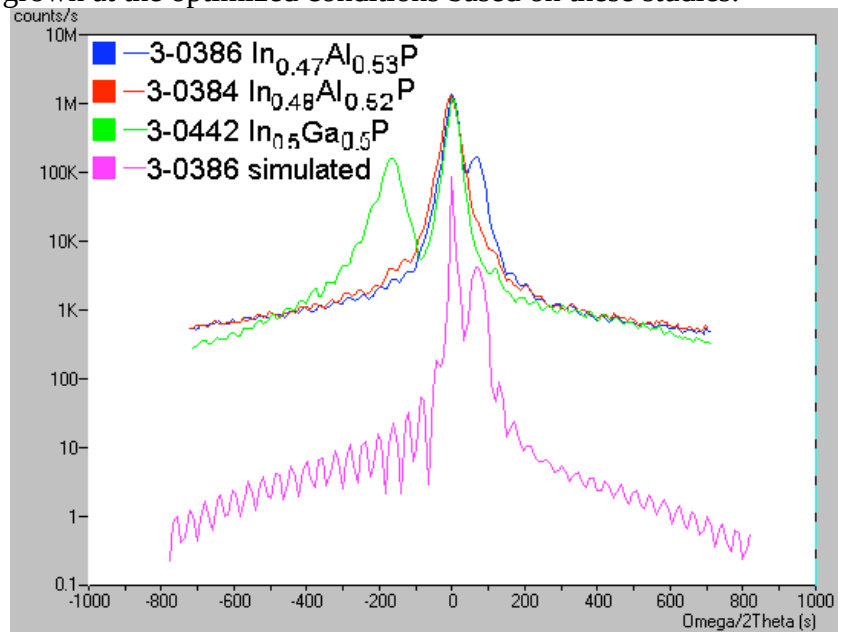

Fig. 1 XRD (004) rocking curves of InGaP, InAlP single layer samples. The sample information is indicated in the figure. The bottom curve is a fitting of the curve measured from sample 3-0386.

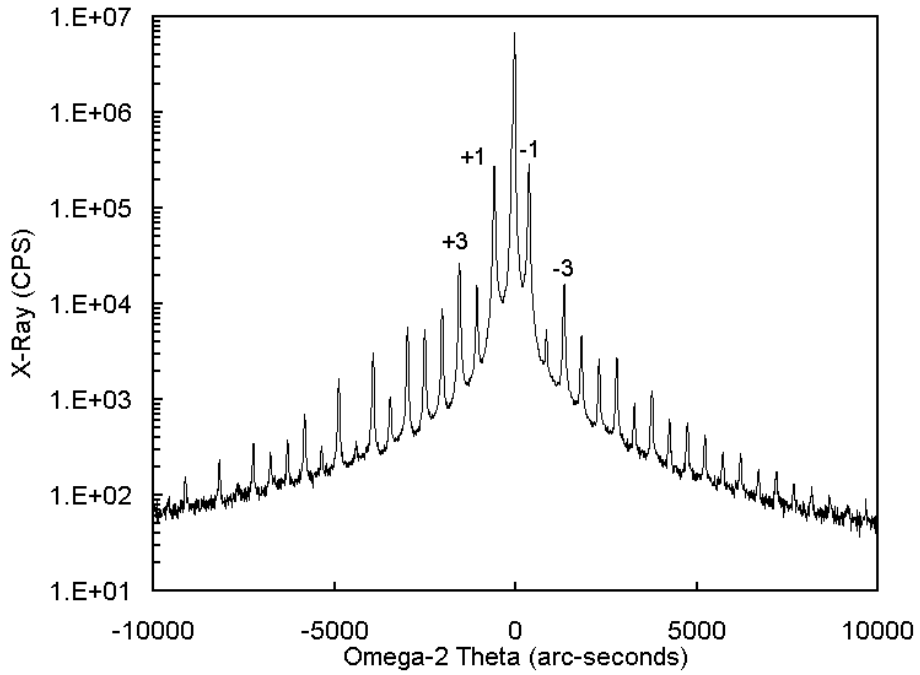

Fig. 2 X-ray (004) ω-2θ scan of a 10-period $In_{0.49}Ga_{0.51}P$ /GaAs SL structure.

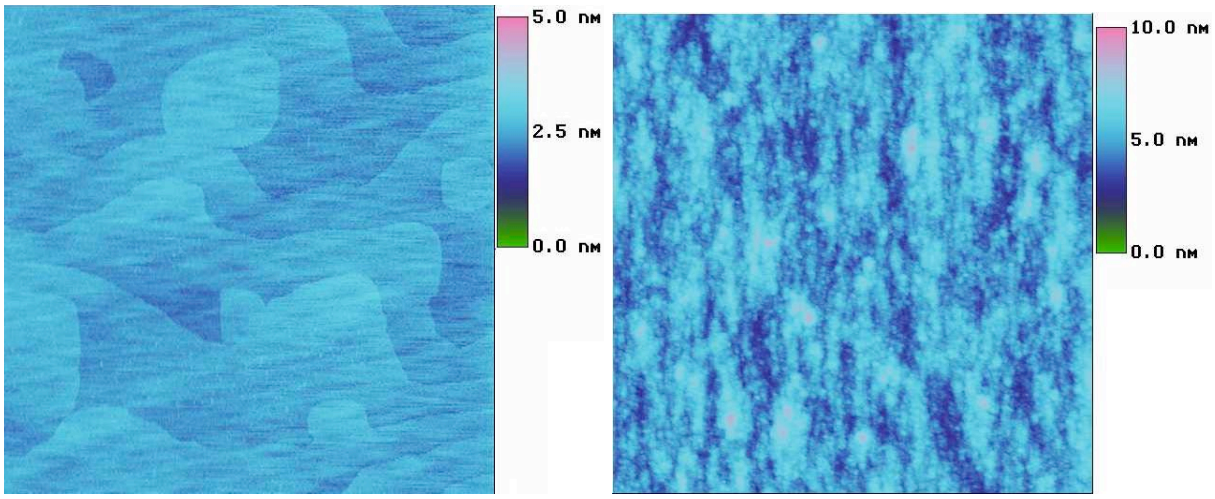

(a) (b)

Fig. 3 AFM images of 450 nm $In_{0.48}Al_{0.48}P$ samples with (a) and without (b) 20 nm thick GaAs cap layer. Image size is 5x5 μm^2 each and vertical scale for each image is shown.

Investigation of InAlP native oxides for Metal-Oxide-Semiconductor device applications

Oral Candidacy Exam

Ying Cao

Department of Electrical Engineering

University of Notre Dame

Advisor: Douglas C. Hall

August, 2005

Contents

1. Introduction

Due to the wide array of high electron mobility alloys of varying bandgaps that can be epitaxially grown on its surface and available semi-insulating substrates, GaAs remains one of the most widely used semiconductors for high-speed optoelectronic applications and wireless communication systems. While Schottky gates are commonly used in high-speed GaAs transistors, the restricted forward bias (a few tenths of a volt) that can be applied without excessive gate leakage currents limits their power handling capability. A metal-insulator-semiconductor field effect transistor (MISFET) has the advantages over a Schottky gate device that it can be operated with higher positive or negative voltages applied to its gate with very low gate leakage current and that its input impedance can be extremely high, being essentially that of the insulator. Since the electrical characteristics of native oxides of GaAs are far inferior to those of SiO_2 on Si, an alternative insulator has long been pursued, such as SiO_2[1], SiON[2], Al_2O_3[3], CaF_2[4], GaS[5], P_3N_5[6] and other insulators[7,8], to enable the preferred metal-insulator-semiconductor gate structure. In recent years, many deposited insulator/GaAs structures have been investigated, although only a few have yielded promising results.[9-12] Native oxide films on GaAs can offer advantages of processing convenience and low cost. Wet thermal oxides of AlGaAs[13] have been studied but found to suffer from midgap traps caused by residual interfacial As.[14] These traps lead to increased interface recombination velocity[15,16] and high leakage currents.[17,18] However, the wet thermal oxides of *As-free* $In_{0.5}Al_{0.5}P$ (lattice matched to GaAs) have been found to possess excellent

insulating[19,20] and interfacial properties[20,21] and may provide a viable native oxide for III-V MOS devices.

To date, thermal wet oxidation of InAlP epitaxial layers and the electrical properties and microstructure of InAlP wet oxides scaled to thicknesses suitable for MOS device applications have been studied in this work. GaAs-based Metal-Oxide-Semiconductor field-effect transistors (MOSFET) with InAlP wet oxides as the gate insulator have been fabricated and characterized. Thermal dry oxidation of InAlP epilayers and the microstructures and electrical properties of InAlP dry oxides have also been studied. Under our proposed future research, GaAs-based MOSFETs with shorter gate lengths and/or thinner InAlP oxides as the gate insulator will be fabricated and characterized.

2. Previous work

2.1 Thermal wet oxidation of InAlP

Native oxides of Al-containing semiconductors such as $Al_xGa_{1-x}As$[13] and $In_{0.5}(Ga_xAl_{1-x})_{0.5}P$[22] have been obtained by oxidation at high temperatures using water vapor. In this research, the thermal wet oxidation of $In_{0.5}Al_{0.5}P$ epitaxial layers grown by metalorganic chemical vapor deposition on GaAs substrates has been studied.

To study the wet oxidation temporal dependence, a relatively thick 600 nm InAlP epitaxial layer has been employed. Following the growth of a 100 nm undoped GaAs buffer layer, the InAlP epilayer is grown and a 50 nm GaAs cap layer is then deposited to protect the underlying InAlP layer from atmospheric oxidation as shown in Fig. 2.1 (a). The samples are put into a 1:5 HCl: H_2O solution to remove the native oxides on the GaAs cap layer and then a 4:1 citric acid: 30% H_2O_2 solution to selectively etch away GaAs cap layers over the InAlP. The samples are then immediately transferred into a 2-in. diameter quartz tube furnace for thermal wet oxidation from the surface. The water vapor is supplied to the furnace with 0.68 l/min of UHP N_2 bubbled through 95 °C H_2O. Several different times (0.5, 1, 1.5 and 2 hours) at different temperatures (420 ºC, 440 ºC, 460 ºC, 480 ºC and 500 ºC) have been investigated.

Unlike AlGaAs oxides which are actually thinner than the semiconductor layer consumed during oxidation, InAlP oxides expand to thicknesses that are on average 50% more than the consumed epilayers as is shown in Fig. 2.1 (b). The InAlP oxide layers have been shown to be composed primarily of mixtures of $InPO_4$

and $AlPO_4$.[23] The thicknesses of InAlP oxides grown from the epilayers have been determined by variable angle spectroscopic ellipsometry (VASE) as shown in Fig. 2.2. Each data point represents one independently oxidized sample.

The growth of oxide can be characterized by the well-known linear parabolic model developed for Si by Deal and Grove.[24] The temporal dependence of the oxide thickness χ_{ox} is given by:

$$\chi_{ox}^2 + A\chi_{ox} = B(t+\tau), \quad (1)$$

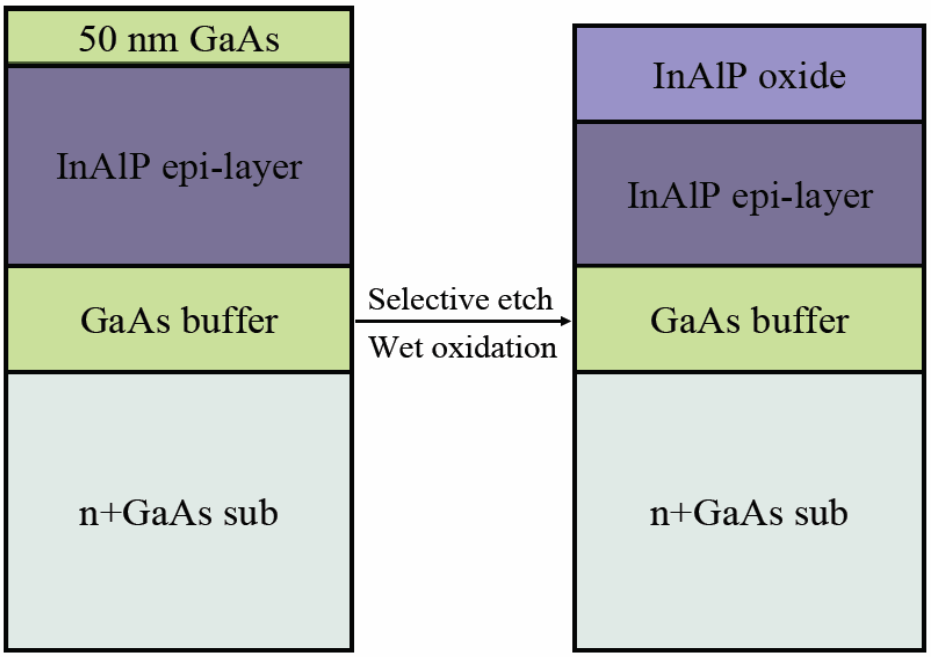

(a) unoxidized (b) oxidized

Figure 2.1. Schematic diagrams of the oxidation of an InAlP epitaxial layer (a) showing the as-grown structure and (b) after being oxidized. The thickness of the InAlP oxide is greater than the InAlP layer thickness measured from the as-grown structure.

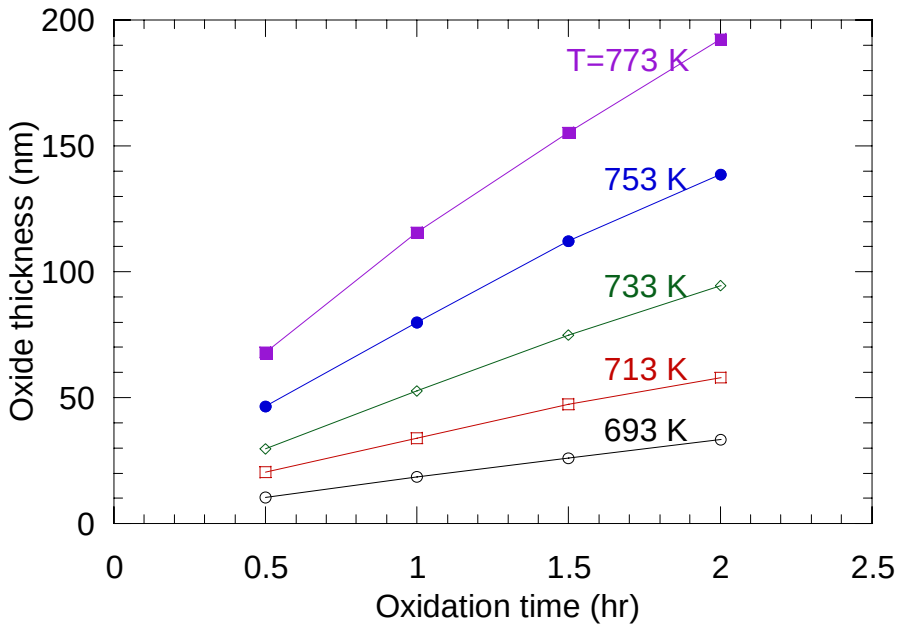

Figure 2.2. Measured oxide thickness as a function of oxidation time at different temperatures.

where B and A are often termed the parabolic and linear rate constants, respectively, and they physically represent the respective contributions of oxidant diffusion and interface reaction mechanisms. From Eq. (1), two limiting forms of the linear parabolic growth law can be seen. When one of the two terms dominates, Eq. (1) reduces to the linear growth (i.e., reaction rate limited) equation

$$\chi_{ox}=B/A(t+\tau) \tag{2}$$

or conversely, the parabolic growth (i.e., diffusion limited) equation:

$$\chi_{ox}^{2}=B(t+\tau). \tag{3}$$

The parameters B/A and B can be extracted for each temperature by fitting the measured oxide growth data in Fig. 2.2 to Eq. (1). The Arrhenius plot for the rate constants B and B/A corresponding to the diffusive and reactive growth mechanisms is shown in Fig. 2.3. Activation energies of 1.52 eV/molecule and 1.16 eV/molecule

are obtained for the diffusive and reactive processes, respectively. As is well known, the thermal oxidation of silicon in water vapor is characterized by activation energies of 0.78 eV/molecule and 2.05 eV/molecule, for the diffusive and reactive mechanisms, respectively.[25] The lower reactive activation energy of InAlP thermal wet oxidation may be due to a lower energy required to break the relatively weak In-P bonds in InAlP[26] which may be the limiting process in the oxidation.[23] Adrian L. Holmes of University of Texas has studied the wet thermal oxidation of InAlP and determined activation energies 0.88 eV/molecule and 0.64 eV/molecule for the diffusive and reactive processes, respectively.[19] The discrepancy between the results of this work and Holmes' study may lie in accuracy of the different instruments used to measure the thicknesses of the oxides. Holmes used scanning electron microscopy, generally considered less accurate for thickness determination, in his experiments. Our VASE technique is described further in the next section.

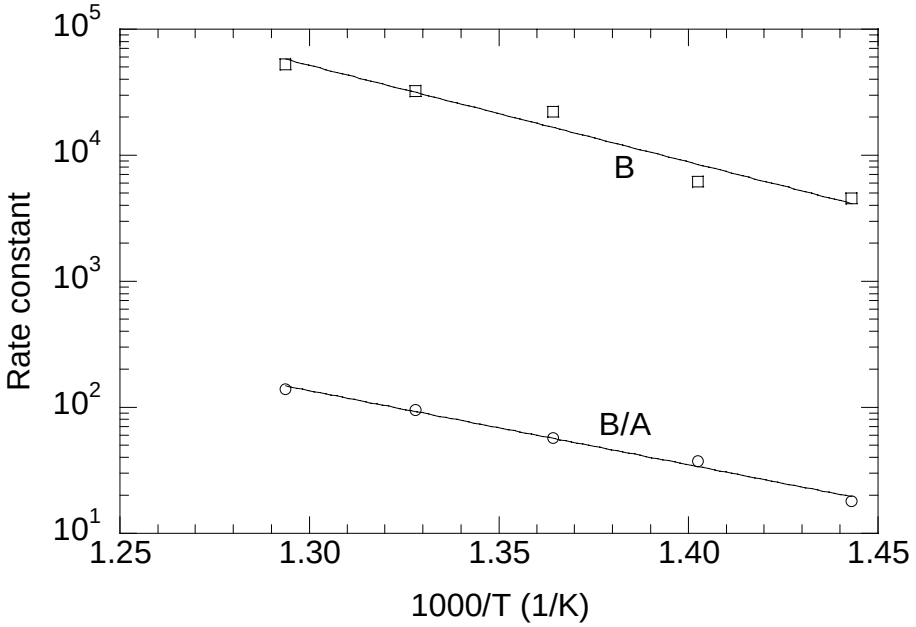

Figure 2.3. Arrhenius plot of the rate constants *B* (diffusive) and *B/A* (reactive). Activation energies of 1.52 eV and 1.16 eV are obtained for the diffusive and reactive rates, respectively.

2.2 Ellipsometric characterization of InAlP wet oxides

Variable angle spectroscopic ellipsometry (VASE) has become a tool used widely for measuring thin film thickness and material optical properties of semiconductors. It is very adaptable to a large variety of materials including metals, dielectrics, semiconductors, and polymers.

The mathematical theory for ellipsometric analysis is based on the Fresnel reflection or transmission equations for polarized light at each boundary between different materials.[27,28] An ellipsometric measurement is typically expressed in terms of an amplitude ratio, psi (Ψ), and a phase quantity, delta (Δ), defined by the complex ratio

$$\rho = \tan(\psi) e^{i\Delta} = \frac{\tilde{R}_p}{\tilde{R}_s}$$

of R_p and R_s which are the complex Fresnel reflection coefficients for p- and s-polarized light.[27] VASE measures the complex ratio, ρ, as a function of both wavelength and angle of incidence. Figure 2.5 illustrates a basic ellipsometric measurement.

For bulk materials, the optical properties can be computed directly from an ellipsometric measurement at a known angle, φ, as:

$$\varepsilon = (n + ik)^2 = \sin(\varphi)^2 \{ 1 + \tan(\varphi)^2 [(1-\rho)/(1+\rho)]^2 \},$$

where ε is the complex dielectric function, n is the real refractive index and k is the imaginary refractive index. However, the equations are much more complicated for single or multilayered films. In this case, the desired parameters must be obtained indirectly by using regression analysis. In other words, an optical model is constructed using as much known information about the sample as possible while unknown parameters, such as film thicknesses and optical constants, are obtained by varying them until the theoretical response closely matches the measured data.

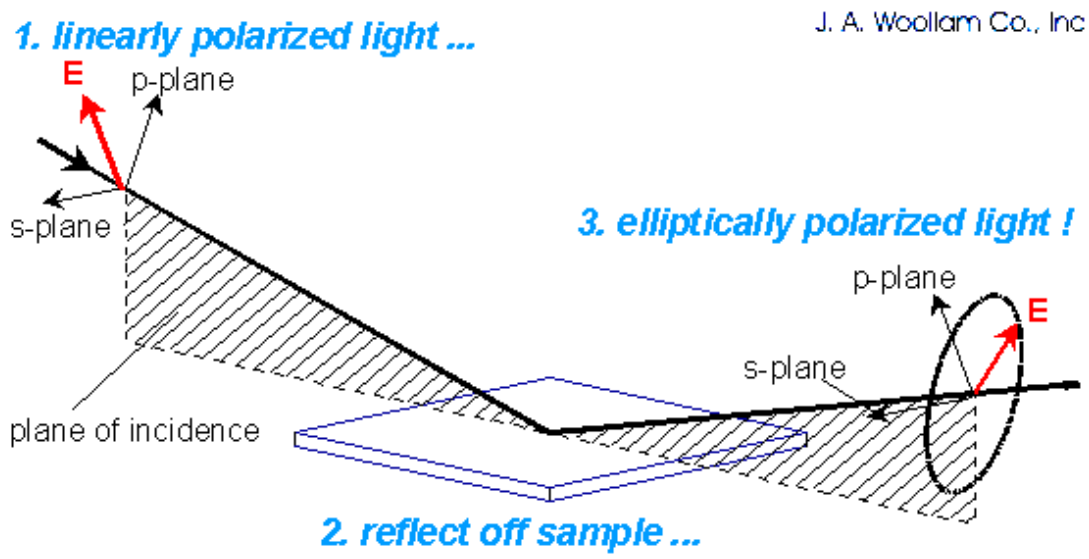

Figure 2.5. Geometry of an ellipsometric measurement. *[Courtesy J. A. Woollam Co., Inc]*

Ellipsometric measurements of this work are all performed using a VASE® system (available wavelength range from 240 nm to 1700 nm) manufactured by J. A. Woollam Co., Inc. An ellipsometric analysis software, WVASE32®, from J. A. Woollam Co., Inc is used for modeling of collected experimental data.

Typical ellipsometric data and fit for a sample are shown in Fig. 2.6. Multiple incident angles, 65°, 70° and 75°, are used to measure the amplitude ratio (Ψ) as shown in Fig. 2.6 (a), and the phase quantity (Δ) as in Fig. 2.6 (b). In a constructed model as

InAlP oxide_Lorentz	110.13 nm
GaAs	1 mm

a Lorentz oscillator[29] is used to characterize the optical properties of InAlP oxide. Based on the constructed model, the sample has a 110 nm InAlP oxide on a GaAs substrate.

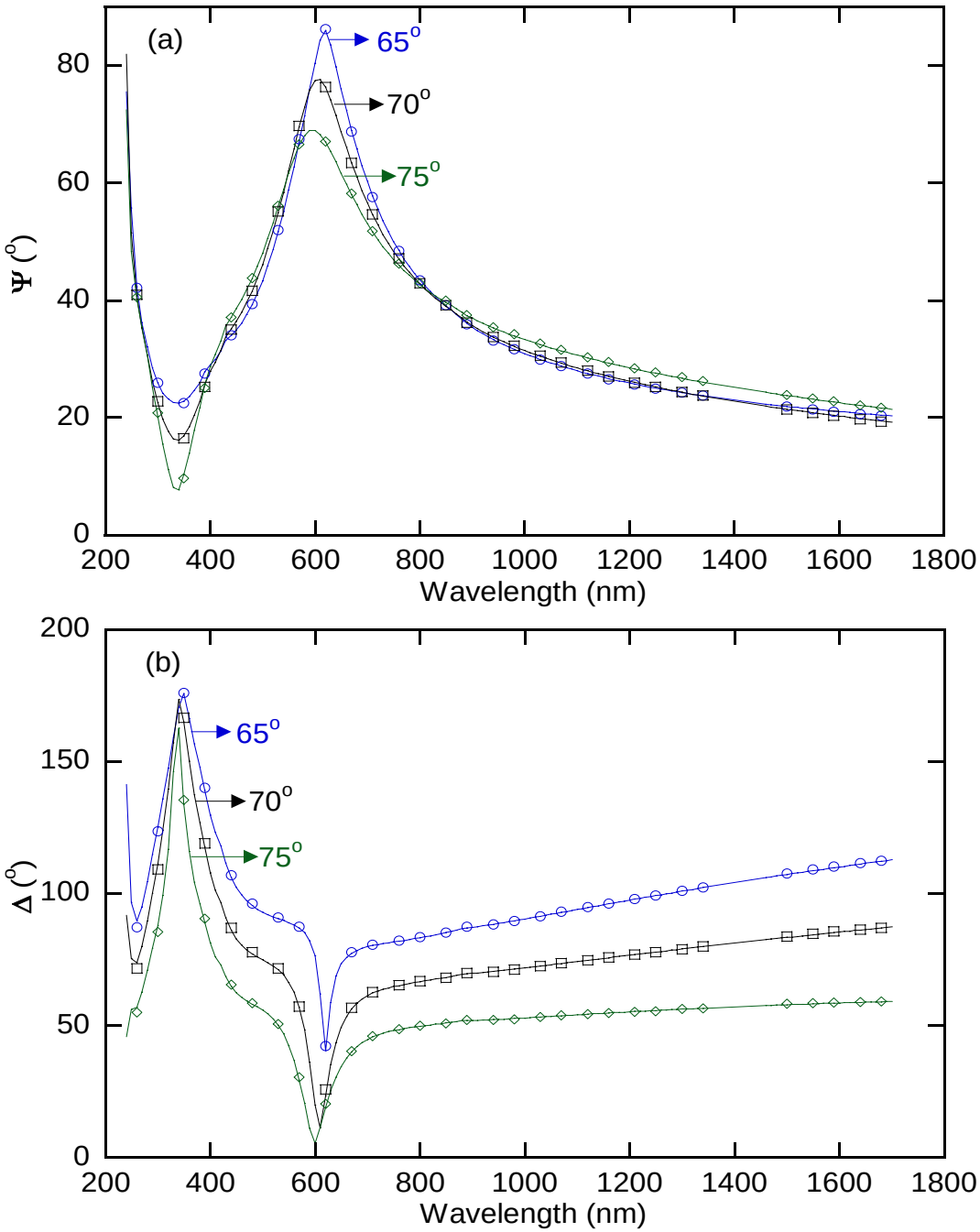

Figure 2.6. Ellipsometric data and fit for a 110 nm InAlP oxide on GaAs substrate for the wavelength range 240 nm–1700 nm. The open circle, open square and open diamond curves represent experimental data collected at incident angles of 65°, 70° and 75°, respectively. The solid lines are fitting curves calculated from the proposed model.

The wavelength-dependent optical constants of the InAlP oxide calculated from the oscillator layer in the model are shown in Figure 2.7. For the wavelength range 600-1700 nm, the oxide has a real refractive index ~1.58 and negligible absorption (imaginary index $k<10^{-3}$). The onset of strong absorption happens at wavelengths below 600 nm.

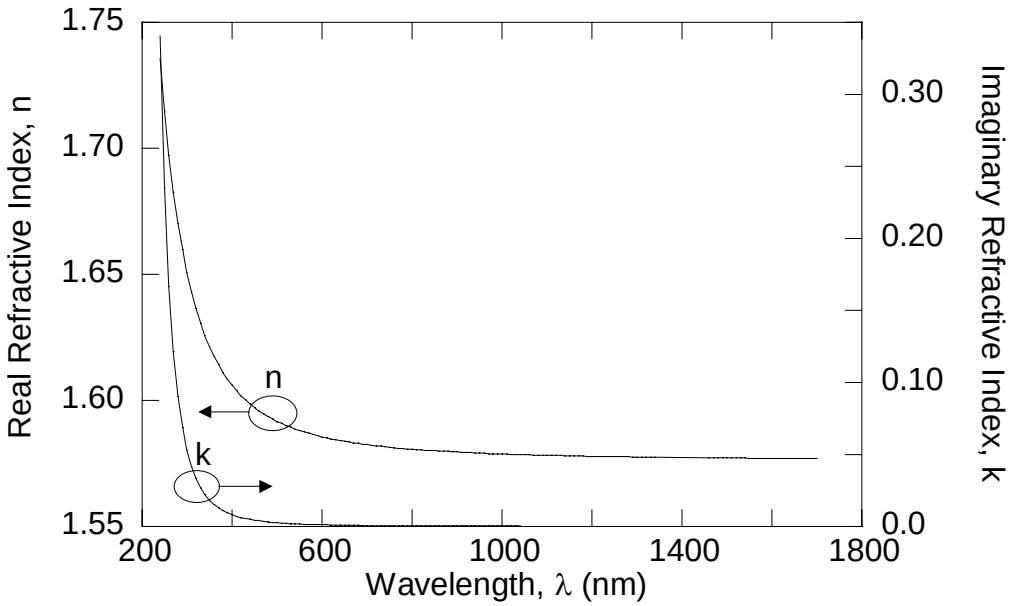

Figure 2.7. Optical constants of InAlP oxide. n remains about 1.58 for λ = 600–1700 nm. Strong absorption appears only at high photon energies corresponding to λ < 600 nm.

For amorphous materials, the absorption coefficient α is known to have the characteristics represented by the Tauc equation[30]

$$(\alpha E_{photon}) = B(E_{photon}-E_g)^2,$$

where $\alpha = 4\pi k/\lambda$, B is a constant and E_g is the optical bandgap. Experimental values of $(\alpha E_{photon})^{1/2}$ are plotted against E_{photon} in Figure 2.8. As the spectral range of our

system is limited to 240–1700 nm, the absorption in the ultra violet region cannot be measured. Thus E_g should be *at least* 4.0 eV as is obtained from the plot in Fig. 2.8.

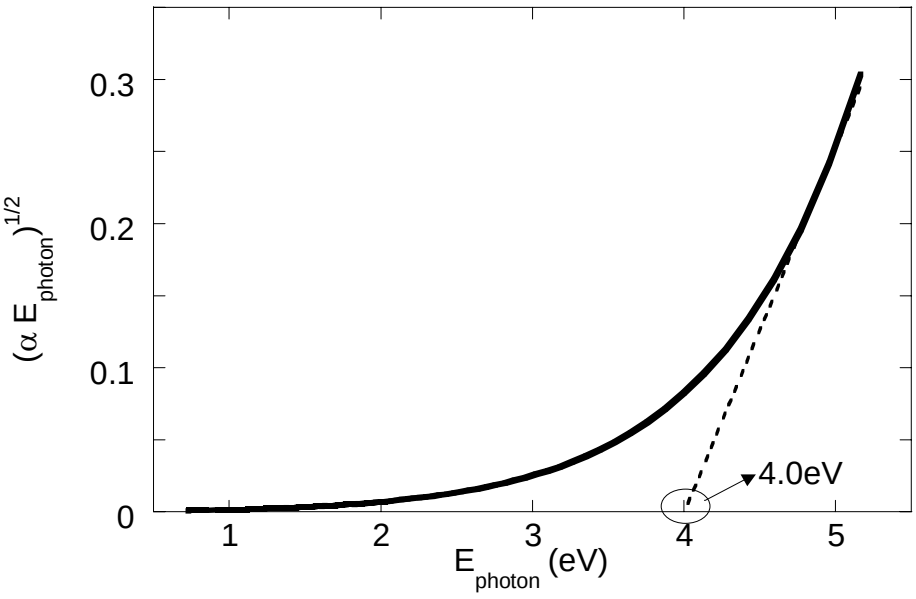

Figure 2.8. The dependence of $(\alpha E_{photon})^{1/2}$ on photon energies from which the optical bandgap E_g is determined to be at least 4.0 eV. A higher value may exist, but measurement at higher photon energies than our instrument can reach are required in order to make the determination.

2.3 Electrical characterization of InAlP wet oxides

Metal-oxide-semiconductor (MOS) capacitors fabricated on different heterostructures have been used to examine the electrical properties of InAlP wet oxides. MOS capacitors on *n*-type heterostructures are fabricated by thermal evaporation of Cr/Au electrodes onto the oxide surface (with three different sizes – 340x340, 240x240 and 120x120 μm^2 − defined by optical lithography) and also onto the entire back of the wafer for ohmic contacts as shown in Figure 2.9 (a). For *p*-type heterostructures, the electrodes are patterned on the oxide surface so that each inner

metal pad (120x120 μm^2) has a surrounding square metal ring (outside border diameter 1200 μm and inside border diameter 140 μm) as shown in Figure 2.9 (b). For two capacitors, C1 and C2, connected in series, the total capacitance C is

$$C = C1*C2 / (C1+C2).$$

Since the area ratio of two capacitors here is 98.64 which determines the capacitance ratio, the total capacitance will be 99% of the capacitance of the capacitor with smaller metal pad area.

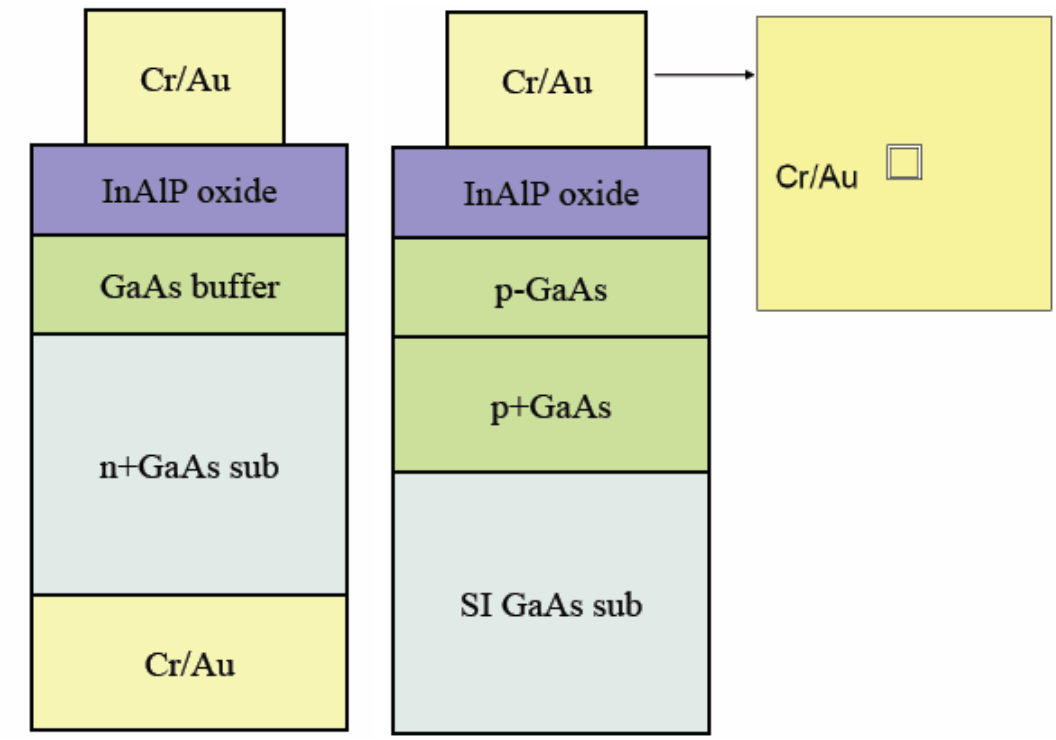

(a) *n*-type (b) *p*-type

Figure 2.9. Schematic diagrams of MOS capacitors fabricated from *n*- and *p*-type heterostructures.

2.3.1 Current-voltage characteristics

Previously at Notre Dame, P. Barrios studied the leakage current density of oxides etch-thinned from a 110 nm oxide as shown in Figure 2.10. Upon etching the fully-oxidized 110 nm InAlP oxide down to 49 nm, the leakage increases slightly (from $9x10^{-11}$ A/cm^2 to $5x10^{-10}$ A/cm^2 at 0.4 MV/cm). However it soars to $2x10^{-7}$ A/cm^2 at 0.4 MV/cm when etching down to 24 nm. The dark particles at the oxide-GaAs interface may contribute to the increased leakage of etch-thinned samples. On the other hand, the etching may cause pinholes in the oxide which lead to the higher leakage current density for etch-thinned oxides. The thickness of the InAlP oxide has to be scaled down for practical MOS applications but etching back from a thick oxide apparently cannot achieve a good quality thin oxide.

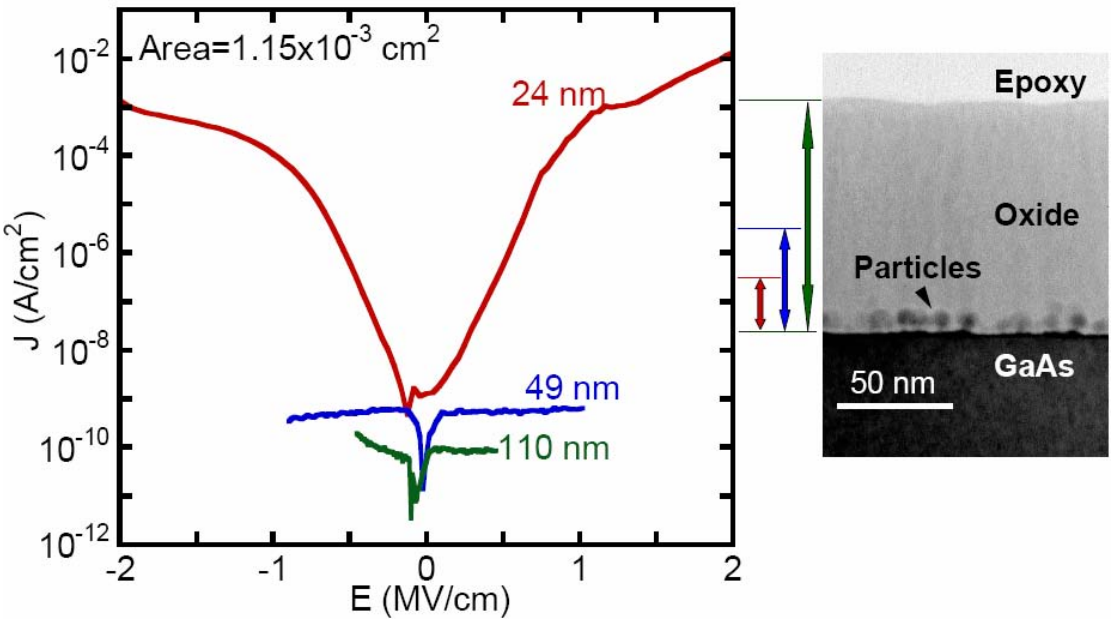

Figure 2.10. Previous study of leakage current density comparison of etch-thinned oxides. *[Courtesy P. Barrios]*

In this work, we have investigated the growth of oxides from thinner as-grown epitaxial InAlP layers. For this study, the *n*-type heterostructures grown on Si-doped ($2x10^{18}$ cm^{-3}) GaAs substrates consist of a 500 nm Si-doped (~10^{16} cm^{-3}) GaAs

buffer layer, an undoped $In_{0.485}Al_{0.515}P$ layer with one of three different thicknesses (63, 31, or 15 nm), and a 50-nm-thick undoped GaAs cap layer. The *p*-type heterostructures are grown on semi-insulating GaAs substrates, and consist of 1000 and 500 nm C-doped GaAs layers ($2x10^{18}$ and $1x10^{17}$ cm^{-3}, respectively), an undoped $In_{0.485}Al_{0.515}P$ layer (63, 31, or 15 nm), and a 50 nm undoped GaAs cap layer.

The GaAs cap layers are removed as described in Section 2.1 and samples are thermally oxidized from the surface in a 500 °C furnace with water vapor. The 63, 31, and 15 nm InAlP layers are fully oxidized (for 65, 30, and 15 minutes, respectively) and expand upon oxidation to corresponding oxide thicknesses (obtained from TEM images) of 110±1.6, 48±1.7, and 17±1.1 nm, respectively. The average expansion factor is about 1.5.

Current-voltage measurements on capacitors made from as-grown oxides are carried out using an Agilent 4156C semiconductor parameter analyzer. As the leakage currents are very small, self calibration and zero cancellation are performed before each measurement to ensure the accuracy.

Figure 2.11 shows a comparison of leakage current density for MOS capacitors fabricated from as-grown and etch-thinned samples with oxides on *n*-type GaAs substrates. Fig. 2.11 (a) shows that at a field of 1 MV/cm, the measured leakage current density, J_L, of the as-grown sample with the 48 nm oxide ($8.7x10^{-11}$ A/cm^2) is about one order of magnitude lower than that of the 49 nm etch-thinned oxide ($6.1x10^{-10}$ A/cm^2). Fig. 2.11 (b) shows that at an electric field of 1MV/cm, leakage current density of the sample with 17 nm as-grown oxide ($1.4x10^{-9}$ A/cm^2) is 6 orders of magnitude below that of 24 nm etch-thinned oxide ($4.0x10^{-4}$ A/cm^2). The

jaggedness appearing in the curve of the 48 nm as-grown oxide in Figure 2.11 (a) results from the 10 fA resolution of the measurement instrumentation. The electric field is obtained by dividing the applied voltage by the measured oxide thickness. Breakdown fields for all InAlP native oxides are in the 3–6 MV/cm range. Table I lists a comparison of these leakage current density and breakdown field results with other native and deposited oxides on GaAs. At the same field strength, the 48 nm InAlP oxide of Figure 2.11 (a) exhibits more than one order of magnitude less leakage than the 64 nm $Gd_{0.31}Ga_{0.1}O_{0.59}/Ga_2O_3$ dielectric stack of Ref. 12. Compared to other candidate insulators on GaAs structures, InAlP native oxides clearly possess the excellent insulating properties needed for MOS device applications.

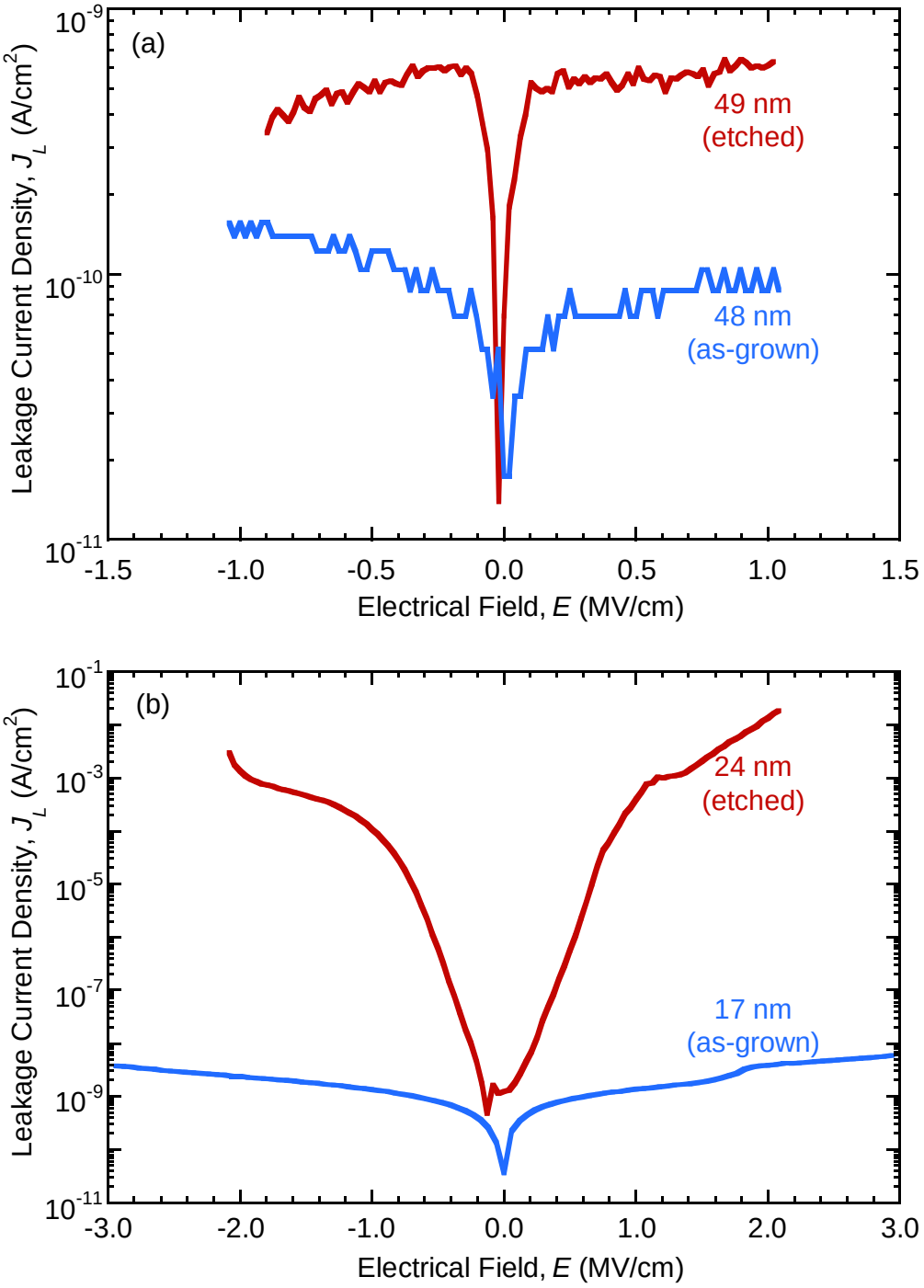

Figure 2.11. Comparison of leakage current density versus electric field curves for MOS capacitors fabricated from as-grown and etch-thinned samples. (a) 48 nm thick InAlP native oxide films on *n*-type GaAs substrates compared to 49 nm etch-thinned oxide and (b) 17 nm native oxide films compared to 24 nm etch-thinned oxide. The leakage current densities of etch-thinned samples were measured by P. Barrios.

TABLE I. Comparison of the leakage current densities, J_L, at applied field of 1 MV/cm (except as noted) and breakdown fields, E_B, for various deposited and native oxide insulators and thicknesses, d, on GaAs. All devices are MOS capacitors except as noted.

Insulator	d (nm)	J_L (A/cm^2)	E_B (MV/cm)	Ref.
$Ga_2O_3(As_2O_3)$ [a]	30	1.2×10^{-4}	5.3	31
$Gd_{0.31}Ga_{0.1}O_{0.59}/Ga_2O_3$	64	1×10^{-9}	3.5	12
Al_2O_3	8	9×10^{-8}	5	10
InAlP oxide	110	9×10^{-11} [b]	6.3	20
Al_2O_3 [a]	16	$<10^{-4}$ [c]	N. R.	11
AlGaAs oxide	45	4.9×10^{-7}	3.8	32
$Ga_2O_3(As_2O_3)$	65	2×10^{-7}	4.7	33
InAlP oxide	48	8.7×10^{-11}	3-6	This work
InAlP oxide	17	1.4×10^{-9}	3-6	This work

[a] MOSFET
[b] Maximum measurement voltage of 5 V (0.45 MV/cm)
[c] Range reported for voltages < 3V (<1.88 MV/cm)
N. R. = not reported

2.3.2 Capacitance-voltage characteristics

Quasi-static and high-frequency (100 kHz) capacitance-voltage (C-V) measurements are performed using a Keithley model 82 C-V measurement system. Figure 2.12 shows capacitance-voltage measurements for the 48 nm oxides and 17 nm oxides on both *n*-type and *p*-type GaAs under standard microscope illumination as is required for wide bandgap semiconductors due to the low thermal generation rate of electron-hole pairs.[34] The clear existence of three operational regimes – accumulation, depletion and inversion – of these MOS structures for both *n*- and *p*-type samples indicates that the Fermi level is unpinned. Thicker oxide (110 nm) on both types of GaAs also shows similar unpinned behavior (not shown). The

frequency dispersion (offset between CQ and CH curves in accumulation) seen in Figure 2.12 is commonly observed[8,34,35] in III-V MOS structures. Possibly attributable to a high density of interface states or a low resistivity interfacial region of the oxide, which reduces the effective oxide thickness and thus increases the apparent capacitance at low measurement frequencies (Maxwell-Wagner effect[34]), it is in general not well understood. Using bias-dependent swept-frequency impedance spectroscopy, a total interface state density of 8×10^{11} cm^{-2} has previously been found for the 110 nm oxide on n-type GaAs.[21] This is comparable to the reported results on other competitive GaAs MIS structures.[8,9,36]

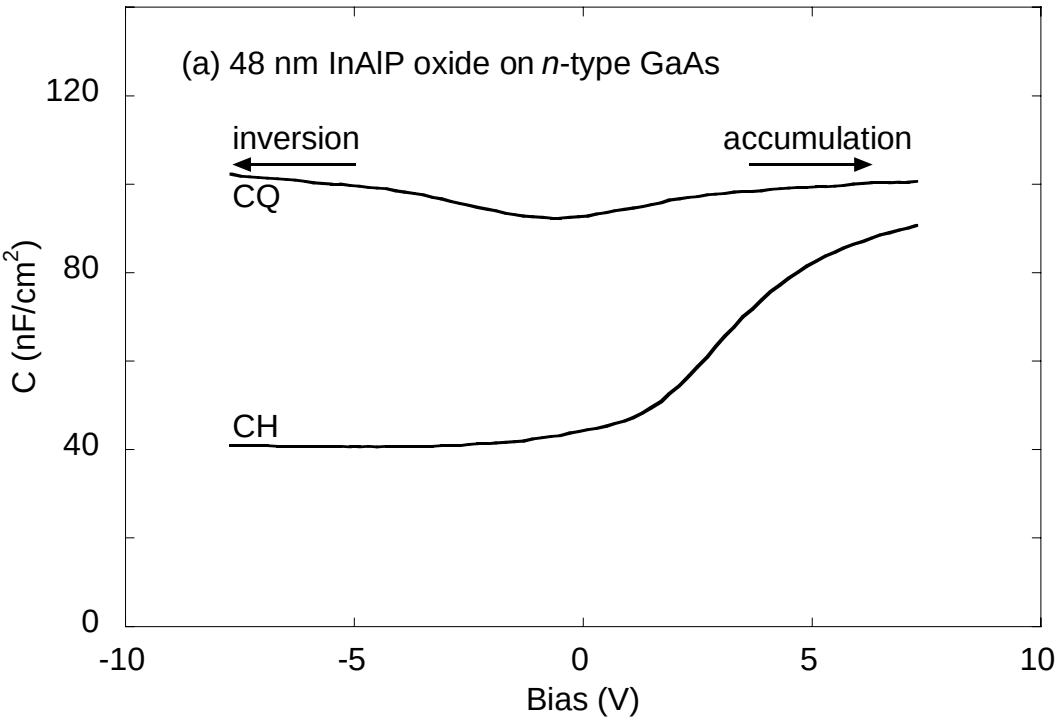

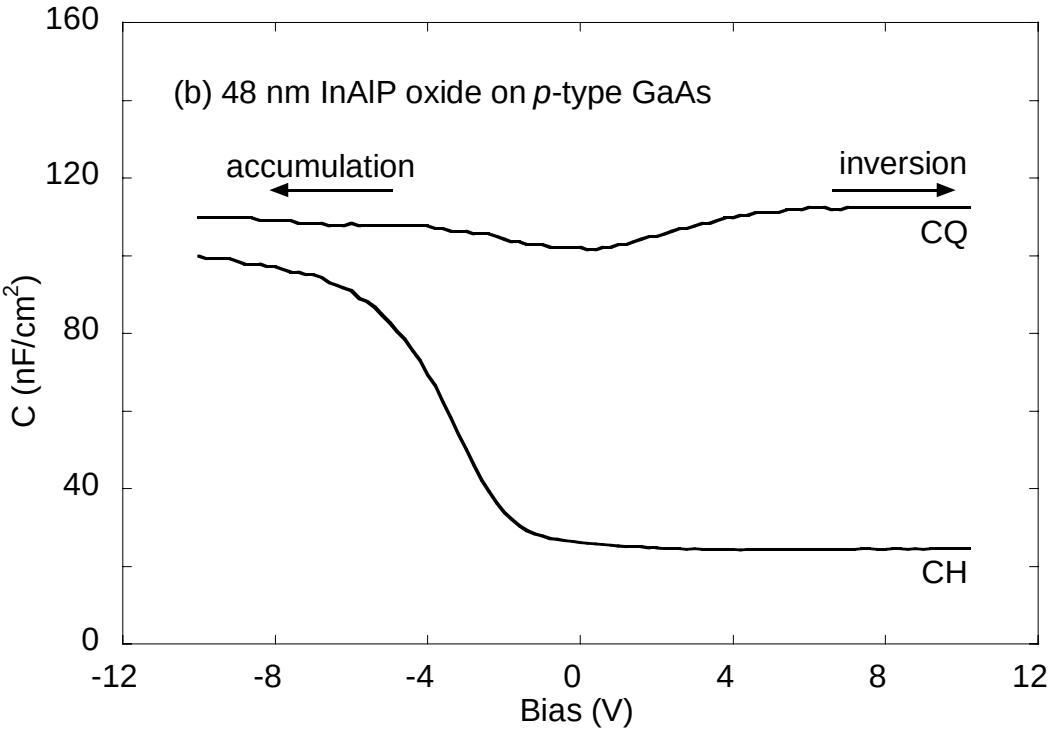
(b) 48 nm InAlP oxide on p-type GaAs
accumulation
inversion
CQ
CH
C (nF/cm2)
Bias (V)
160
120
80
40
0
-12
-8
-4
0
4
8
12

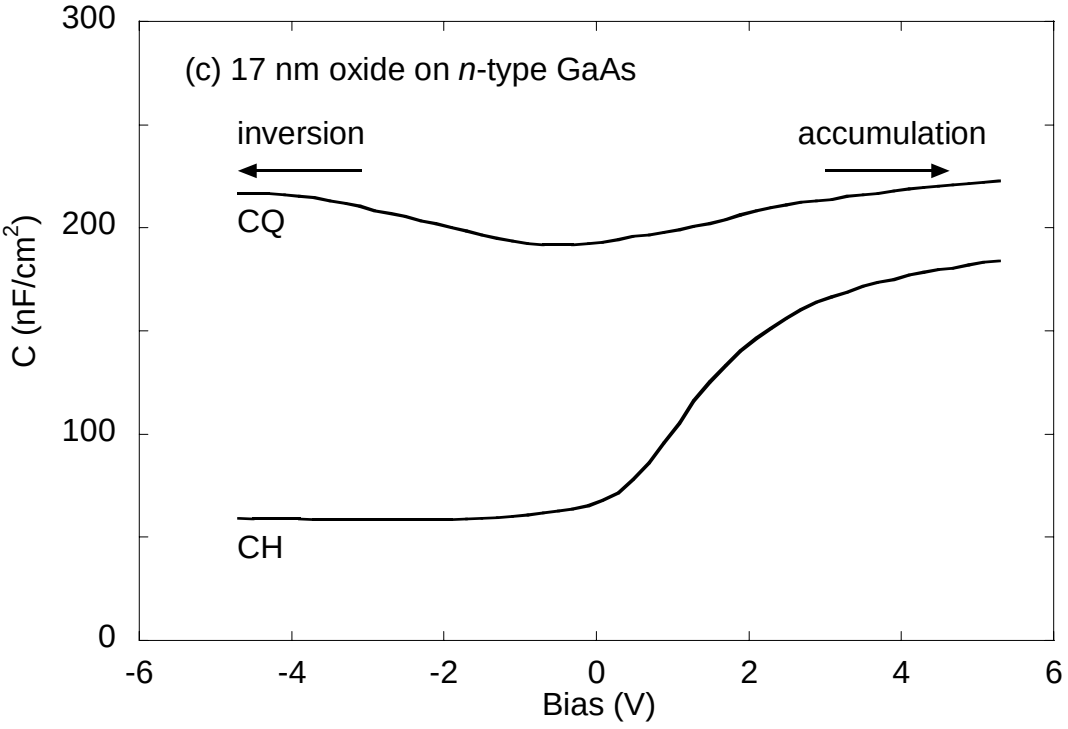
(c) 17 nm oxide on n-type GaAs
inversion
accumulation
CQ
CH
C (nF/cm2)
Bias (V)
300
200
100
0
-6
-4
-2
0
2
4
6

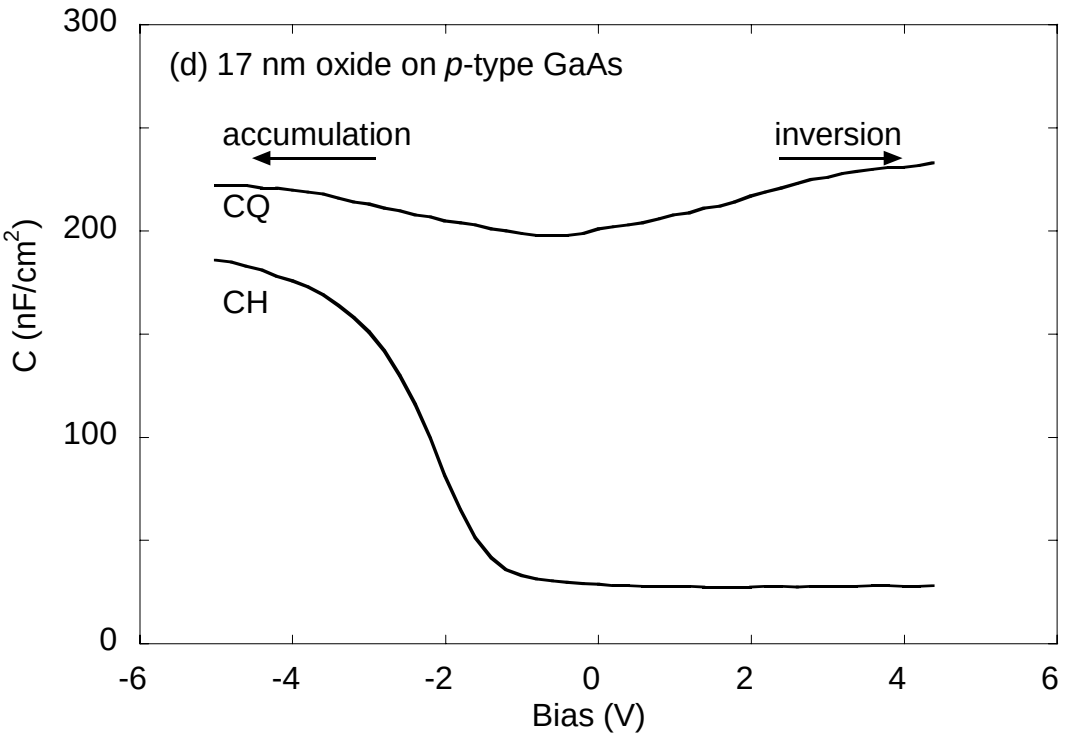

Figure 2.12. High-frequency (CH, 100 kHz) and quasi-static (CQ) capacitance-voltage measurements for 48 nm native oxide of InAlP on (a) *n*-type and (b) *p*-type GaAs and 17 nm oxide on (c) *n*-type and (d) *p*-type GaAs . Sweep rate is 50 mV/s. CQ data show inversion for both carrier types, indicating an unpinned Fermi level.

2.4 Transmission electron microscopy (TEM) of InAlP wet oxides

TEM cross-sectional specimens are prepared by standard methods of mechanical pre-thinning (with dimple grinding or wedge polishing) followed by 2 kV Ar-ion milling.

The bright-field TEM images of two fully oxidized samples with different oxide thicknesses (110 nm and 17 nm) are shown in Figure 2.13. Dark particles are observed near the oxide/GaAs interface in the 110 nm oxide of Figure 2.13 (a), while no dark interfacial particles appear in the 17 nm oxide of Figure 2.13 (b). Figure 2.13 (b) is representative of the entire observable area for this and a second wedge-

polished cross section specimen, with the absence of particles also confirmed for plan-view specimens (not shown) in which possible loss of particles due to ion milling and electron beam interactions is suppressed by the fact that they are protected from the vacuum by the substrate and overlying oxide film. The interfacial particles in Figure 2.13 (a) are believed to be indium rich based on Z-contrast TEM images[37] (not shown) and Auger depth profiling.[38] The size of the particles increases with the progressive consumption of the InAlP epilayer during oxidation.[37] One possible hypothesis is that during oxidation, elements in the semiconductor epilayer migrate to the sample surface and react with oxidants. Indium, the heaviest element in the structure, outdiffuses more slowly than the other alloy constituents and hence may accumulate near the interface during oxide growth, forming In-rich particles.

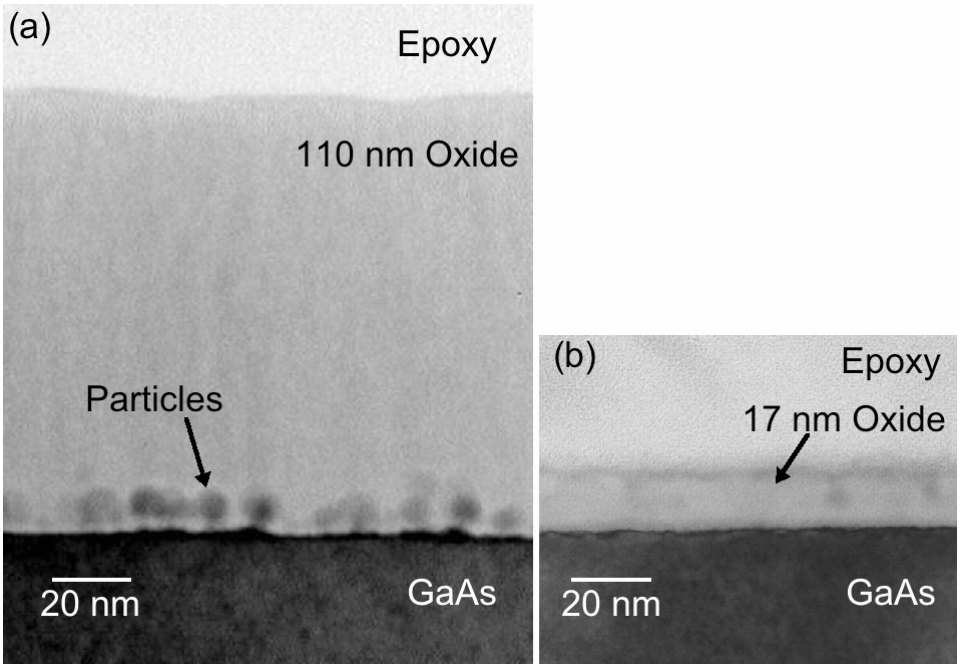

Figure 2.13. Comparison of bright field TEM images of (a) 110 nm and (b) 17 nm thick InAlP wet thermal native oxide films. The particles clearly visible in (a) are not present anywhere in sample (b). *[Courtesy J. B. Jasinski, Z. Liliental-Weber, J. Zhang and T. Kosel]*

2.5 Fabrication of MOSFETs based on InAlP wet oxides

The excellent electrical properties of InAlP wet oxides, as discussed in Section 2.3, make them a potential MIS gate insulator material. The first functional MOSFET using InAlP wet oxides as gate insulators were fabricated by Li.[39,40] Due to inferior material properties of the heterostructures, the earlier MOSFET devices suffer from a 55–79% decrease of channel doping after any thermal process (including oxidation) as shown in Table II. Therefore the DC (direct current) and RF (radio frequency) performance of the device is severely degraded. Carrier concentration data are obtained from Van de Pauw measurements[41] performed on samples after different thermal processes.

Table II. Effects of thermal processes on first generation MOSFET heterostructures.

	Temperature (ºC)	Time (min)	Carrier concentration (cm^{-3})	Mobility (cm^2/v-s)
As-grown	–	–	1.06×10^{17}	4000
Wet oxidation[40]	440	25	2.23×10^{16}	3029
Annealing in oxidation furnace with N_2	440	10	3.96×10^{16}	3523
Annealing in RTP with N_2	440	1	4.26×10^{16}	3279
Annealing in RTP with forming gas	440	1	4.03×10^{16}	3500

Heterostructures obtained more recently from another crystal grower (Epiworks, Inc.) do not have the severe problem of channel doping reduction after thermal treatment. The fabrication procedure of new MOSFETs fabricated from these heterostructures, and the improved DC and RF performance of the devices, will be discussed in detail in the following sections.

2.5.1 Fabrication procedure

The fabrication of the first functional MOSFET consisted of an entire-surface oxidation followed by wet-etching for mesa isolation.[39,40] Due to the sidewalls created during wet etching, it is hard to prevent the gate metal from overlapping the mesa edge thus creating a parasitic leakage path to the channel[42]. To reduce the gate leakage caused by sidewalls and excessive processing of gate oxides and improve the quality of the ohmic contacts of the device, a new procedure was later developed[40] to include regional oxidation and implant isolation. Although the fabricated MOSFET has greatly improved performance, it cannot be fully pinched off due to imperfect implant isolation. It also suffers from the doping reduction of the channel because of crystal growth problems.

Wet-etching mesa isolation and regional oxidation are combined in this work to fabricate MOSFETs on an Epiworks heterostructure (MOSFET1) grown by metal-organic chemical vapor deposition (MOCVD) as shown in Fig. 2.14. A GaAs buffer layer is first grown on a semi-insulating GaAs substrate, followed by a 100-nm Si-doped GaAs channel layer (N_d ~ 1-2 x 10^{17} cm^{-3}), a 4-nm undoped $In_{0.5}Ga_{0.5}P$

oxidation stop layer, 15 nm of Si-doped (N_d ~ 1 x 10^{18} cm^{-3}) $In_{0.5}Al_{0.5}P$ lattice-matched to GaAs and a 50-nm heavily Si-doped GaAs cap layer (N_d > 2 x 10^{18} cm^{-3}).

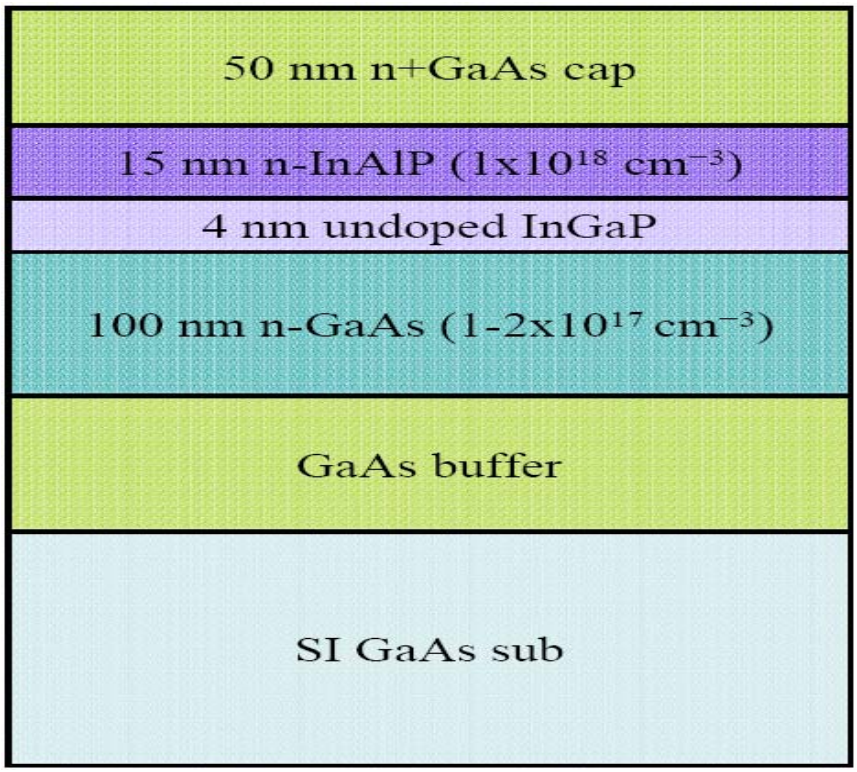

Figure 2.14. Schematic diagram of the heterostructure (MOSFET1) grown by Epiworks, Inc.

Solvent cleaning is first performed on the heterostructures before further processing. Mesas for device isolation are defined by optical lithography and formed with several wet etching steps. The GaAs cap layer is first removed by selective wet etching in a citric acid and hydrogen peroxide solution (Citric: H_2O_2 = 10:1). The InAlP and InGaP epilayers are etched away by an HCl solution (HCl:H_2O = 2:1), then the citric peroxide solution is used again to etch through the GaAs channel and into the buffer layer.

Thereafter, the gate regions of MOSFETs are also defined using lithography and the GaAs cap layers in the gate regions are selectively etched away by the citric

peroxide solution for regional oxidation, carried out at 440 ºC for 30 minutes. The oxide thickness is calibrated to be 15 nm from VASE on an entire-surface oxidized sample with the same oxidation conditions.

After oxidation, source and drain regions are defined and formed by thermal evaporation of AuGe (88% Au, 12% Ge)/Ni/Au. The ohmic contacts are then obtained by rapid thermal annealing. Annealing conditions are optimized by utilizing a TLM (transfer length method) sample undergoing the same wet-etching mesa isolation and regional oxidation as each MOSFET sample. Typically, best quality ohmic contacts are obtained by annealing at 400 ºC for 20 seconds in a nitrogen ambient.

Gate patterns are defined and Cr/Au metal gates are deposited using thermal evaporation and liftoff. The nominal source-to-gate and drain-to-gate distance of all fabricated devices is 1 μm, and the gate widths vary as 20, 50, 100 and 150 μm. MOSFETs with gate lengths from 1 to 8 μm were fabricated. The cross section of a complete device is shown in Fig. 2.15.

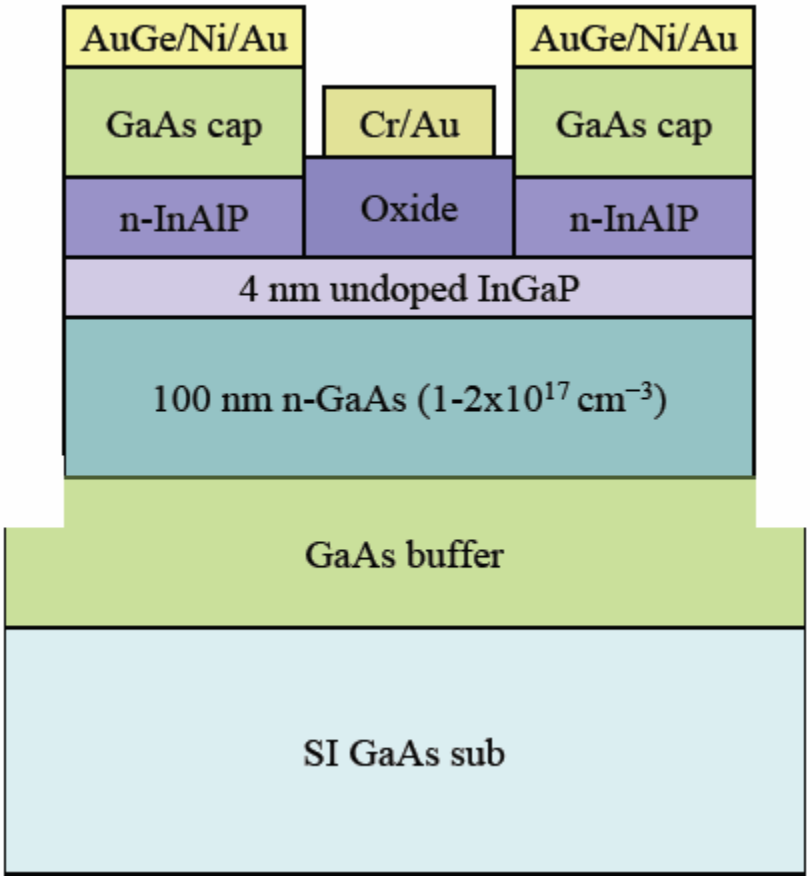

Figure 2.15. Schematic cross-section diagram of a MOSFET.

2.5.2 DC characteristics of fabricated MOSFETs

The DC performance of the fabricated "50x2" MOSFETs (i.e., shorthand designation for a unit gate width of 50 μm and two gate fingers) with a 1-μm gate length, and of MOSFETs made by evaporating gate metals, with gate lengths of 3, 4, 6, and 8 μm, to the regions between two TLM pads (gate width of 100 μm) are characterized using an Agilent 4155C semiconductor parameter analyzer. Fig. 2.16 shows a typical common source drain current characteristic measured from a 1 μm gate length device.

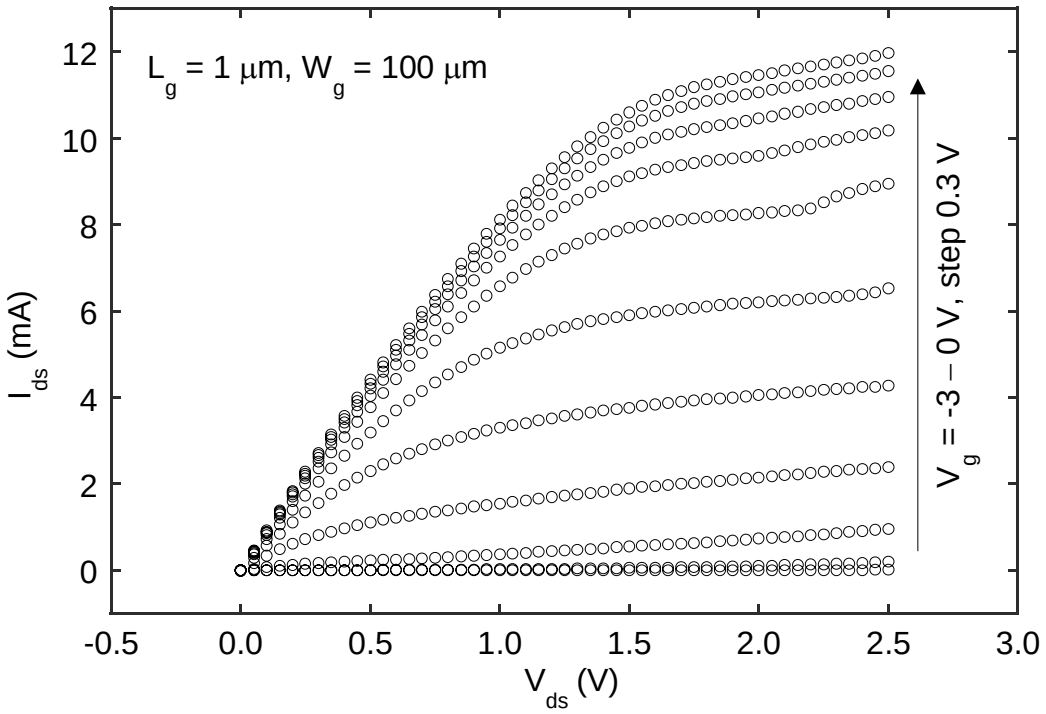

Figure 2.16. Drain current as a function of drain voltage measured from a 50 x 2 MOSFET with the gate length of 1 μm.

A transfer characteristic for one of the fabricated 1 μm devices is shown in Fig. 2.17, where a maximum extrinsic transconductance ($g_{m,max}$) of 73.6 mS/mm is measured at a drain voltage (V_{ds}) of 2 V and a gate voltage (V_{gs}) of −1.44 V.

The DC characteristics show a clear pinch-off at V_{gs} = −3 V and channel modulation with depletion-mode operation. The devices with gate lengths of 3, 4, 6, and 8 μm have similar pinch-off and channel modulation behavior (not shown).

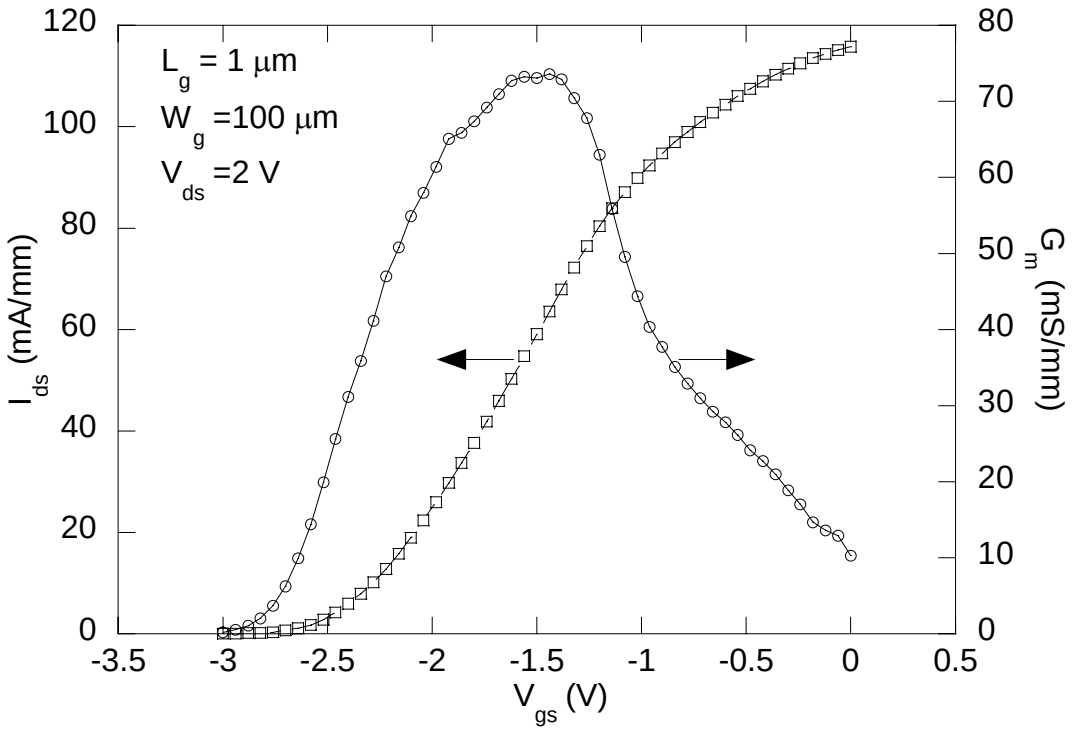

Figure 2.17. The open square line is drain current vs gate bias. The open circle line is extrinsic transconductance vs gate bias. Both are measured from a 50 x 2 MOSFET in the saturation region biased at V_{ds} = 2 V.

A channel sheet resistance of 1863 Ω/sq is obtained by using TLM. From the gate length dependence of R_s calculated from sheet resistance and contact resistance, the intrinsic transconductance can be estimated using:

$$g_{m,int} = g_{m,ex}/(1 - g_{m,ex}R_s),$$

where $g_{m,ex}$ and $g_{m,int}$ are the extrinsic and intrinsic transconductances, respectively. Fig. 2.18 shows the peak extrinsic and intrinsic transconductance versus gate length of MOSFETs with 1, 3, 4, 6, and 8 μm gate lengths. As shown in Fig. 2.18, the calculated peak intrinsic transconductance improved from 36.5 mS/mm for an 8 μm gate length to 80.9 mS/mm at a gate length of 1 μm, and the $g_{m,int}$ follows closely the expected $1/L_g$ trend.

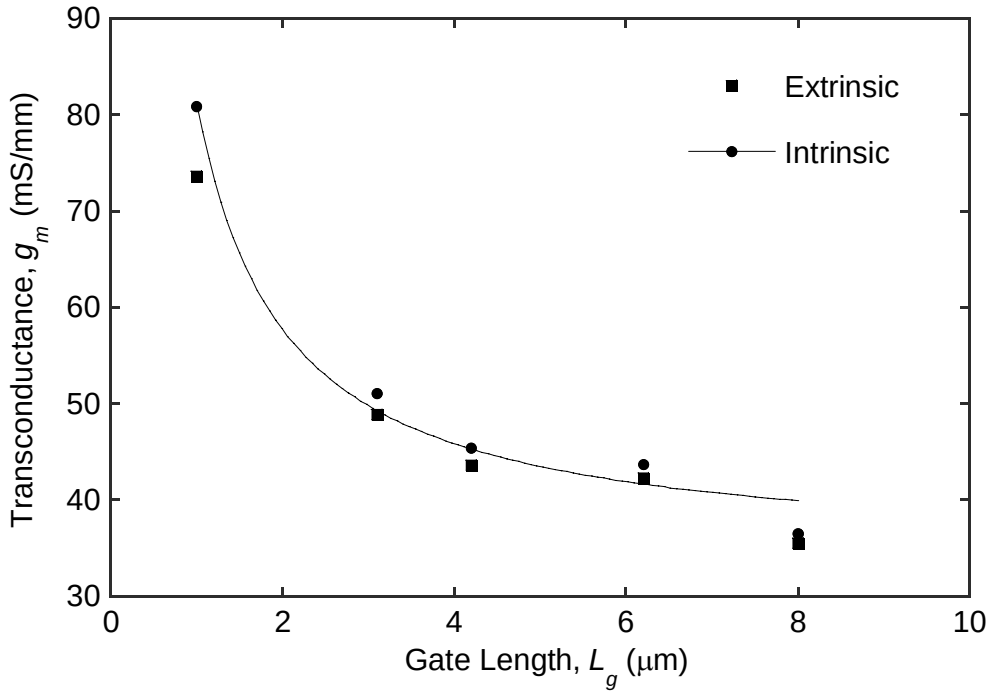

Figure 2.18. Peak extrinsic and intrinsic transconductance for different gate lengths. The gate width is 100 μm for all the devices. Solid line shows $1/L_g$ trend.

The typical gate leakage current of the MOSFETs is shown in Figure 2.19. The typical gate leakage of the MOSFETs with 15 nm gate oxides is essentially larger than the leakage of the capacitors with 17 nm oxide as shown in Fig. 2.11 although the area of the capacitors is much larger than that of the MOSFETs. This may be attributed to the parasitic leakage path along the mesa edge.[42] Ion implant will be needed to improve the isolation.

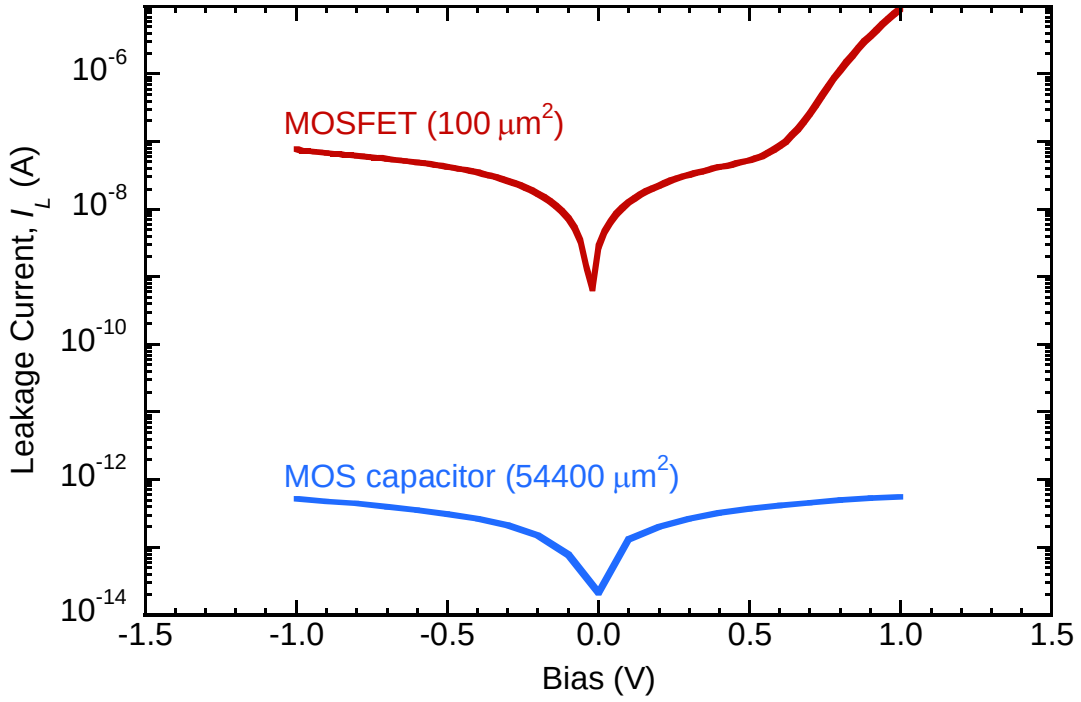

Figure 2.19. Comparison of leakage current of MOSFETs and MOS capacitors with similar oxide thicknesses.

2.5.3 RF characteristics of fabricated MOSFETs

Scattering parameters (S-parameters) are widely used to characterize the high frequency properties of semiconductor devices. Considering a MOSFET as a two-port network with gate-source as port 1 and drain-source as port 2, S-parameters of the MOSFETs with gate length of 1 μm have been measured in a frequency range of 1−35 GHz using a Agilent HP8722 40GHz network analyzer.

The most important figures of merit characterizing a transistor's high frequency performance are the cutoff frequency, f_t, and the maximum oscillation frequency, f_{max}. The cutoff frequency defined as the frequency at which the magnitude of h_{21} equals unity, while the maximum oscillation frequency means the frequency at which MAG reach unity.

Scattering parameters have been measured on the same device whose DC performance is shown in Fig. 2.16 and Fig. 2.17. The frequency response for short-circuit current gain h_{21} and a maximum available gain (MAG) are obtained by biasing the device at V_{ds}=2 V and V_{gs}=−1.5 V. Therefore the cutoff frequency (f_t) and the maximum frequency of oscillation (f_{max}) are determined to be 13.7 GHz and 37.6 GHz by extrapolating h_{21} and MAG, respectively, as shown in Fig. 2.20.

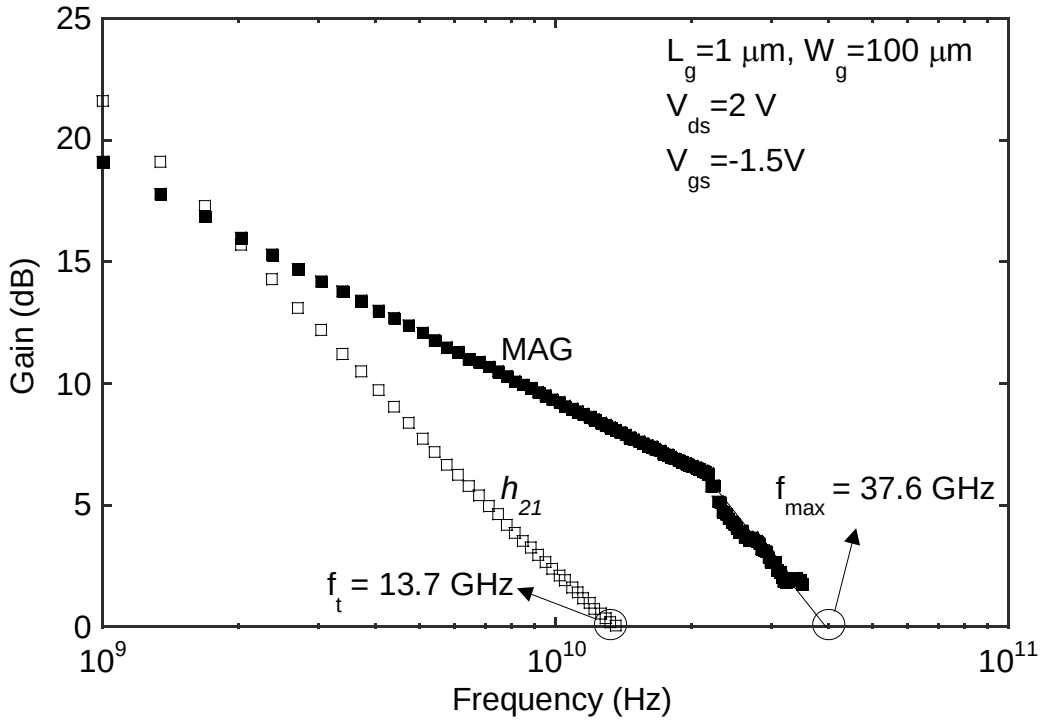

Figure 2.20. MAG and h_{21} vs frequency measured from a MOSFET with f_{max} and f_t estimated from the extrapolations.

2.5.4 Discussion

Compared to the first generation MOSFETs fabricated by Li[39], the MOSFETs fabricated in this work benefit from better material properties so that the performance of the device does not suffer from the reduction of channel doping and is comparable to depletion-mode GaAs MOSFETs with similar gate length reported recently.[43-45]

2.6 Ellisometric study of InAlP dry oxides

In the wet oxidation of III-As compound semiconductors, especially AlGaAs,[46] the hydrogen provided as a byproduct of reactions with the water vapor is known to play an important role in reducing the arsenic oxide intermediate product to volatile arsenic or AsH_3 molecules which then escape from the oxidizing crystal.[47] AlGaAs layers shrink upon wet oxidation because most of the column V element (As) is eliminated, with less than 2% As in the oxide films.[48] In contrast, most of the column V element (P) in InAlP films upon wet oxidation remains in the film as phosphates.[23] It brings the role (if any) of hydrogen during wet oxidation into question and serves as a motivation to explore the dry oxidation of InAlP films.

In this work, the dry oxidation of InAlP epitaxial layers on GaAs substrates has been performed. The oxides formed by dry oxidation have been investigated by VASE and transmission electron microscopy.

The study of the temporal dependence of dry oxidation was performed using the heterostructures grown on semi-insulating GaAs substrates, consisting of 1000 nm and 500 nm C-doped GaAs layers ($2x10^{18}$ cm^{-3} and $1x10^{17}$ cm^{-3}, respectively), an undoped $In_{0.485}Al_{0.515}P$ layer (63 nm), and a 50 nm undoped GaAs cap layer.

The GaAs cap layers are removed by the same method described in Section 2.1 before samples are transferred into the furnace for thermal dry oxidation from the surface for different times (10 minutes, 90 minutes and 180 minutes) at three different temperatures (380 ºC, 440 ºC and 500 ºC). The UHP O_2 is supplied to the furnace with a flow rate of 0.5 l /min. For comparison, wet oxidation on the heterostructures is also performed at 500 ºC for 10 minutes and 50 minutes, respectively.

The ellipsometric data of samples after oxidation under different conditions have been obtained using VASE. Fig. 2.21 displays the comparison of typical ellipsometric data (with incident angle of 70º) of dry oxides ((a) and (b)) and wet oxides ((c) and (d)) all formed at 500 ºC. The comparison of data with other incident angles is similar (not shown). Both Ψ and Δ of wet oxides as shown in Fig. 2.21 (c) and (d), respectively, show drastic changes as the oxidation time vary from 10 minutes to 50 minutes. As the optical properties of wet oxides (n and k) should not change dramatically with oxidation time, VASE data provides evidence that the thicknesses of oxides with different oxidation times are different. From the models constructed for wet oxides, the thicknesses of oxides are determined to be 21 nm and 102 nm for oxidation times of 10 minutes and 50 minutes, respectively. For dry oxides, no VASE data fitting models have been successfully developed to characterize their thicknesses and their optical properties. However, it is observed that Ψ and Δ data for samples dry-oxidized at the same temperature but with different times does not vary significantly as that of wet oxides does. Fig. 2.21 (a) and (b) shows for comparison the Ψ and Δ data for samples with dry oxidation times of 10 minutes and 180 minutes. Therefore it may be reasonably concluded that no significant changes of dry oxide thickness are caused by varying the oxidation time beyond some point near 10 minutes, suggesting formation of a terminal thickness oxide. For samples dry-oxidized at different temperatures from 380 ºC to 500 ºC for the same oxidation time (10 minutes), the variation of Ψ and Δ is also insignificant indicating that the terminal thickness dry oxide formation is rapid even at lower oxidation temperatures (data not shown).

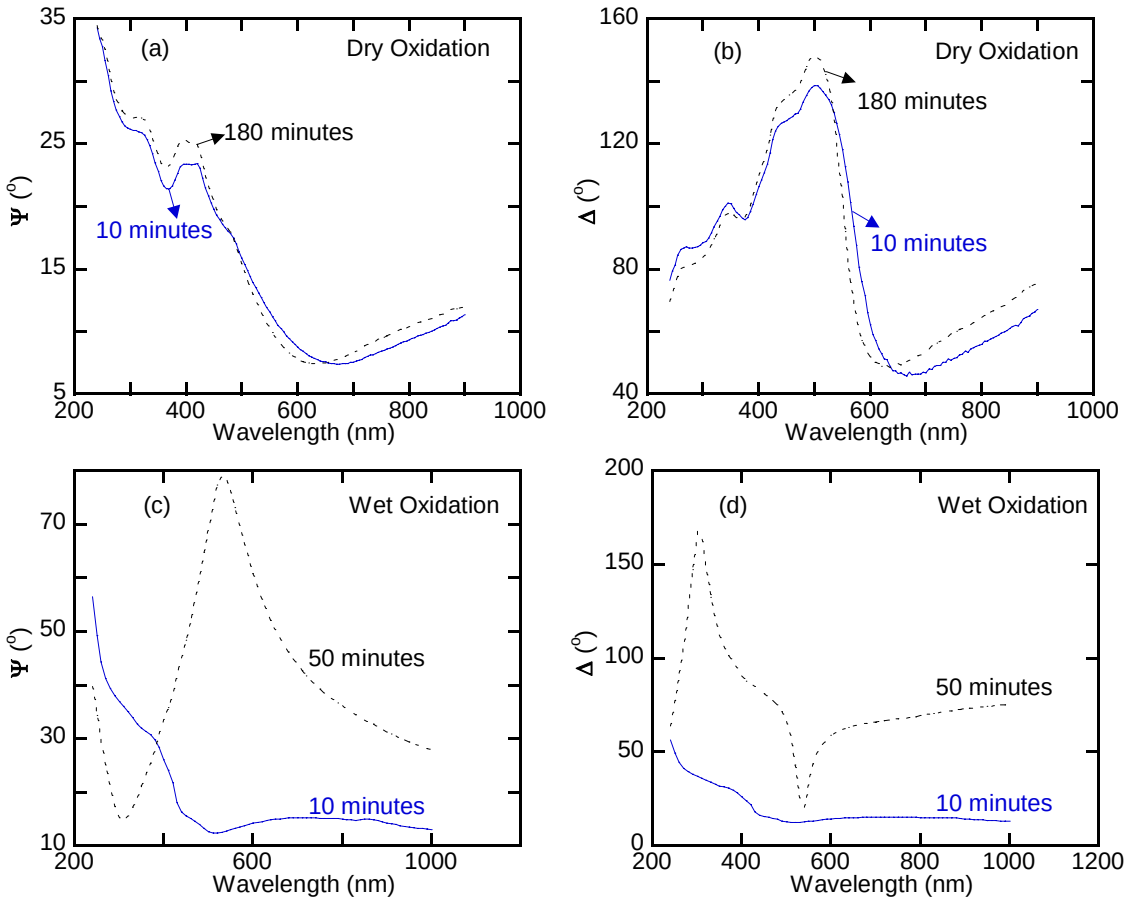

Figure 2.21. Ellipsometric data of dry oxidation with different oxidation time (10 minutes and 180 minutes), and wet oxidation with different oxidation time (10 minutes and 180 minutes). The oxidation temperature is 500 ºC. The incident angle of VASE measurement is 70º.

2.7 Transmission Electron Spectroscopy (TEM) of InAlP dry oxides

TEM cross-sectional specimens of dry-oxidized InAlP samples are made by the same method as discussed in Section 2.4 in order to further analyze the unusual oxidation behavior revealed by the VASE data in section 2.6. Figure 2.22 shows bright field TEM images of dry oxides with (a) 10 minute and (b) 180 minute oxidation time at 500 ºC. These TEM images show that oxides formed by dry oxidation for 10 minutes or longer at different temperatures each have a layer of dark

particles on top. This is in contrast to wet thermal oxides as shown in Fig. 2.13 (a) where a layer of dark particles is formed at the interface between the oxide and the semiconductor. Increasing the oxidation time does not change the thickness of the dry oxides significantly although the majority of the InAlP epilayer remains unoxidized.

The dark particles seen on top of the dry oxides in Fig. 2.22, which seem to form at the early stage of the oxidation, appear to effectively "block" the further dry oxidation resulting in the dry oxides reaching a terminal thickness very fast. It is proven that these particles are also In-rich based on Z-contrast images and energy dispersive X-ray spectroscopy.[49] The mechanism of dry oxidation may be different from the hypothesis of wet oxidation discussed in Section 2.3, and the difference between dry and wet oxidation in the positions where the dark particles form is not yet fully understood.

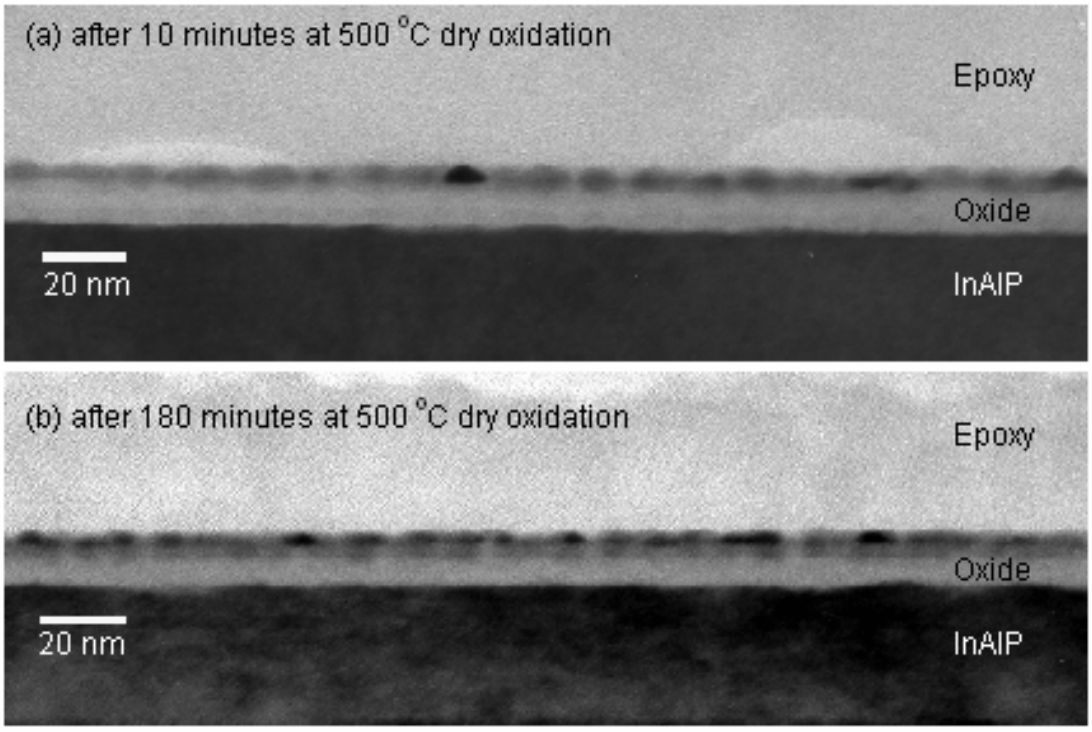

Figure 2.22. Bright field TEM images of dry oxides formed at 500 ºC for (a) 10 minutes and (b) 180 minutes, respectively. *[Courtesy J. Zhang and T. Kosel]*

2.8 Electrical Characterization of InAlP dry oxides

To explore the electrical properties of InAlP dry oxides, MOS capacitors similar to those discussed in Section 2.3.1 are fabricated using an *n*-type heterostructure with 15 nm undoped InAlP epilayer. After GaAs cap layer removal, samples are oxidized at 500 ºC for 10 minutes resulting in an oxide thickness of ~20 nm as determined from TEM imaging.

Fig. 2.23 shows a comparison of typical leakage current density versus bias voltage for capacitors fabricated from both wet and dry oxidized InAlP. Under low biases less than 1 V, the leakage current density of the dry-oxide seems comparable to that of the wet-oxide, while at 5 V its leakage current density is three orders of magnitude higher. The electrical properties of dry oxides were found to vary from

sample to sample, which may be due to the oxide thickness variation caused by the noncontinuous top layer of dark particles as observed from TEM images. Based upon these characterization results, it would appear that InAlP dry oxides are not suitable for MOS device applications.

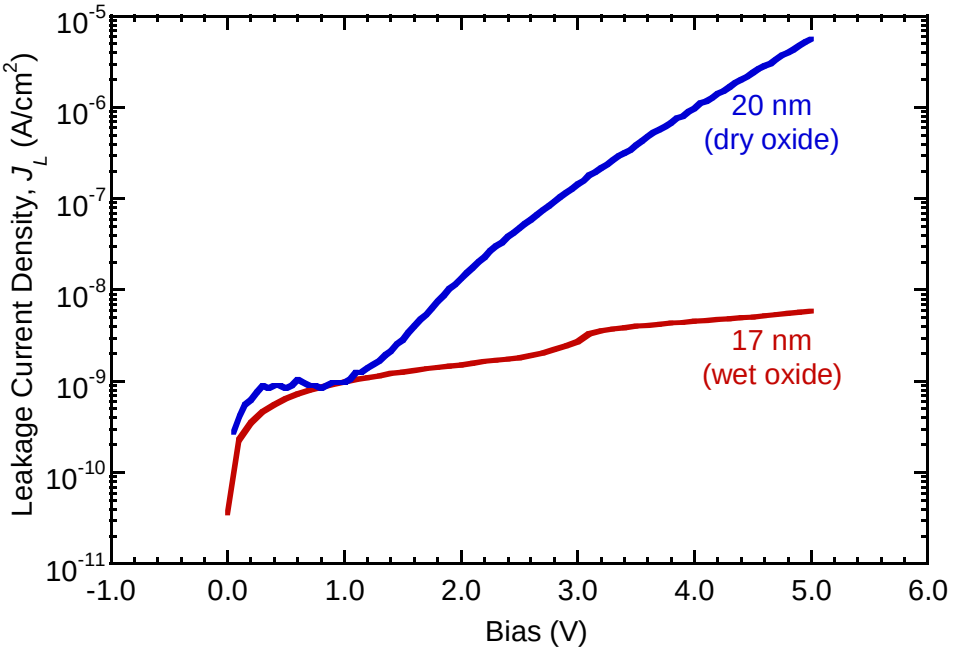

Figure 2.23. Leakage current density comparison between MOS capacitors fabricated from both wet and dry oxidized InAlP.

3. Proposed future work

3.1 Fabrication and characterization of MOSFETs using ion implant for device isolation

To eliminate the possible parasitic leakage path caused by wet-etching mesa isolation, ion implant will be used to separate devices for fabrication of MOSFETs. The conditions for ion implant will be optimized to yield best device performance. The DC and RF performance of MOSFETs will be characterized.

3.2 Fabrication and characterization of MOSFETs with submicrometer gates

Short gate length and small gate resistance are essential factors for high-gain and low-noise performance. MOSFETs with gate length in the range of 0.1 μm to 0.5 μm will be fabricated and investigated. In order to accomplish such short gate lengths, e-beam lithography will be employed for gate definition. A T-shaped gate electrode will be utilized to minimize gate resistance.

3.3 Fabrication and characterization of MOSFETs with thinner gate oxides

The transconductance of a MOSFET is proportional to the gate capacitance.[50] Reduction of thickness of gate oxide will increase the gate capacitance, thus improve the transconductance of a MOSFET.

FET structures with 7.5 nm InAlP epi layers (thus yielding thinner wet thermal oxides upon oxidation) have been obtained from Epiworks, Inc. On such heterostructures, MOSFETs will be fabricated and investigated.

3.4 Other possible future work

Interfacial properties of 110 nm oxides on GaAs have been studied using impedance spectroscopy.[21] Impedance spectroscopy can be used to characterize the interface traps of thinner oxides on GaAs.

Current transient spectroscopy (CTS) measurements can be performed on FET devices to investigate traps encountered by carriers flowing through the channel.

4. References

[1] H. Becke, R. Hall, and J. White, Solid-State Electron. **8** (813) (1965).

[2] L. Messick, J. Appl. Phys. **47** (12), 5474-5475 (1976).

[3] S. Yokoyama, K. Yukitomo, M. Hirose, Y. Osaka, A. Fischer, and K. Ploog, Surf. Sci. **86** (JUL), 835-840 (1979).

[4] T. Waho and F. Yanagawa, IEEE Electron Device Lett. **9** (10), 548-549 (1988).

[5] P. P. Jenkins, A. N. Macinnes, M. Tabibazar, and A. R. Barron, Science **263** (5154), 1751-1753 (1994).

[6] Y. H. Jeong, K. H. Choi, and S. K. Jo, IEEE Electron Device Lett. **15** (7), 251-253 (1994).

[7] T. Mimura and M. Fukuta, IEEE Trans. Electron Devices **27** (6), 1147-1155 (1980).

[8] C. W. Wilmsen, (Plenum, New York, 1985).

[9] M. Passlack, J. K. Abrokwah, R. Droopad, Z. Y. Yu, C. Overgaard, S. I. Yi, M. Hale, J. Sexton, and A. C. Kummel, IEEE Electron Device Lett. **23** (9), 508-510 (2002).

[10] P. D. Ye, G. D. Wilk, B. Yang, J. Kwo, S. N. G. Chu, S. Nakahara, H. J. L. Gossmann, J. P. Mannaerts, M. Hong, K. K. Ng, and J. Bude, Appl. Phys. Lett. **83** (1), 180-182 (2003).

[11] P. D. Ye, G. D. Wilk, B. Yang, J. Kwo, H. J. L. Gossmann, M. Hong, K. K. Ng, and J. Bude, Appl. Phys. Lett. **84** (3), 434-436 (2004).

[12] M. Passlack, N. Medendorp, S. Zollner, R. Gregory, and D. Braddock, Appl. Phys. Lett. **84** (14), 2521-2523 (2004).

[13] J. M. Dallesasse, N. Holonyak, Jr., A. R. Sugg, T. A. Richard, and N. El-Zein, Appl. Phys. Lett. **57**, 2844-2846 (1990).

[14] P. Parikh, Ph. D. Thesis, UC Santa Barbara, 1998.

[15] S. S. Shi, E. L. Hu, J. P. Zhang, Y. I. Chang, P. Parikh, and U. Mishra, Appl. Phys. Lett. **70** (10), 1293-1295 (1997).

[16] M. R. Islam, R. D. Dupuis, A. P. Curtis, and G. E. Stillman, Appl. Phys. Lett. **69** (7), 946-948 (1996).

[17] Carol I. H. Ashby, John P. Sullivan, Paula P. Newcomer, Nancy A. Missert, Hong Q. Hou, B. E. Hammons, Michael J. Hafich, and Albert G. Baca, Appl. Phys. Lett. **70** (18), 2443-2445 (1997).

[18] E. I. Chen, Nick Holonyak, Jr., and S. A. Maranowski, Appl. Phys. Lett., 2688-2690 (1995).

[19] A. L. Holmes, Ph. D. Thesis, University of Texas at Austin, 1999.

[20] P. J. Barrios, D. C. Hall, G. L. Snider, T. H. Kosel, U. Chowdhury, and R. D. Dupuis, in *State-of-the-Art Program on Compound Semiconductors (SOTAPOCS XXXIV), Electrochem. Soc. Proc.* (2001), Vol. 2001-1, pp. 258-264.

[21] X. Li, Y. Cao, D. C. Hall, P. Fay, X. Zhang, and R. D. Dupuis, J. Appl. Phys. **95** (8), 4209-4212 (2004).

[22] F. A. Kish, S. J. Caracci, N. Holonyak, J. M. Dallesasse, A. R. Sugg, R. M. Fletcher, C. P. Kuo, T. D. Osentowski, and M. G. Craford, Appl. Phys. Lett. **59** (3), 354-356 (1991).
[23] D. Pulver, C. W. Wilmsen, D. Niles, and R. Kee, Journal of Vacuum Science and Technology B **19** (1), 207-214 (2001).
[24] B. E. Deal and A. S. Grove, J. Appl. Phys. **36**, 3770-3778 (1965).
[25] J. D. Plummer, M. D. Deal, and P. B. Griffin, *Silicon VLSI technology: fundamentals, practice and modeling*. (Upper Saddle River, New Jersey, 2000), p.817.
[26] F.A. Kish, S.J. Caracci, N. Holonyak, Jr., K.C. Hsieh, J.E. Baker, S.A. Maranowski, A.R. Sugg, J.M. Dallesasse, R.M. Fletcher, C. P. Kuo, T. D. Osentowski, and M. G. Craford, J. Electron. Mater. **21**, 1133-1139 (1992).
[27] R. M. A. Azzam and N. M. Bashara, *Ellipsometry and polarized light*. (North-Holland Pub. Co., New York, NY, 1977), pp.xvii, 529.
[28] Eugene Hecht and Alfred Zajc, *Optics*. (Addison-Wesley Pub. Co., Reading, Mass., 1974), pp.viii, 565.
[29] J. A. Woollam Co., *Guide to Using WVASE32*. (Lincoln, NE).
[30] P. Y. Yu and M. Cardona, in *Fundamentals of semiconductors: physics and materials properties* (Springer, Berlin, NY, 2001), pp. 566-568.
[31] J. Y. Wu, P. W. Sze, Y. H. Wang, and M. P. Houng, Solid-State Electron. **45** (12), 1999-2003 (2001).
[32] P. J. Barrios, S. K. Cheong, D. C. Hall, N. C. Crain, G. L. Snider, C. B. DeMelo, T. Shibata, B. A. Bunker, U. Chowdhury, R. D. Dupuis, G. Kramer, and N. El-Zein, presented at the 42nd Electronic Materials Conference, Denver, Colorado, 2000 (unpublished).
[33] J. Y. Wu, H. H. Wang, Y. H. Wang, and M. P. Houng, IEEE Electron Device Lett. **20** (1), 18-20 (1999).
[34] M. Passlack, M. Hong, J. P. Mannaerts, R. L. Opila, S. N. G. Chu, N. Moriya, F. Ren, and J. R. Kwo, IEEE Trans. Electron Devices **44** (2), 214-225 (1997).
[35] L. G. Meiners, Journal of Vacuum Science and Technology **15** (4), 1402-1407 (1978).
[36] D. G. Park, M. Tao, J. Reed, K. Suzue, A. E. Botchkarev, Z. Fan, G. B. Gao, S. J. Chey, J. Vannostrand, D. G. Cahill, and H. Morkoc, J. Cryst. Growth **150** (1-4), 1275-1280 (1995).
[37] Y. Cao, J. Zhang, X. Li, T. H. Kosel, P. Fay, P. Barrios, D. C. Hall, R. E. Cook, X. Zhang, and R. D. Dupuis, presented at the 46th Electronic Materials Conference, Notre Dame, Indiana, 2004 (unpublished).
[38] M. J. Graham, S. Moisa, G. I. Sproule, X. Wu, J. W. Fraser, P. J. Barrios, D. Landheer, A. J. SpringThorpe, and M. Extavour, Materials at High Temperatures **20** (3), 277-280 (2003).
[39] X. Li, Y. Cao, D. C. Hall, P. Fay, B. Han, A. Wibowo, and N. Pan, IEEE Electron Device Lett. **25** (12), 772-774 (2004).
[40] X. Li, Ph. D. dissertation, University of Notre Dame, 2005.
[41] D. K. Schroder, *Semiconductor Material and Device Characterization*. (Wiley, New York, 1998).

[42] S. R. Bahl, M. H. Leary, and J. A. Delalamo, IEEE Trans. Electron Devices **39** (9), 2037-2043 (1992).
[43] Y. C. Wang, M. Hong, J. M. Kuo, J. P. Mannaerts, J. Kwo, H. S. Tsai, J. J. Krajewski, Y. K. Chen, and A. Y. Cho, IEEE Electron Device Lett. **20** (9), 457-459 (1999).
[44] B. Yang, P. D. Ye, J. Kwo, M. R. Frei, H. J. L. Gossmann, J. P. Mannaerts, M. Sergent, M. Hong, K. K. Ng, and J. Bude, IEEE GaAs Digest (2002).
[45] P. D. Ye, G. D. Wilk, J. Kwo, B. Yang, H. J. L. Gossmann, M. Frei, S. N. G. Chu, J. P. Mannaerts, M. Sergent, M. Hong, K. K. Ng, and J. Bude, IEEE Electron Device Lett. **24** (4), 209-211 (2003).
[46] J. M. Dallesasse, N. Holonyak, A. R. Sugg, T. A. Richard, and N. Elzein, Appl. Phys. Lett. **57** (26), 2844-2846 (1990).
[47] Carol I. H. Ashby, John P. Sullivan, Kent D. Choquette, K. M. Geib, and Hong Q. Hou, J. Appl. Phys. **82** (6), 3134-3136 (1997).
[48] R. D. Twesten, D. M. Follstaedt, and K. D. Choquette, in *Vertical-Cavity Surface Emitting Lasers*, edited by K. D. Choquette and D. G. Deppe (1997), Vol. 3003, pp. 55-61.
[49] T. H. Kosel and J. Zhang, 2005 (unpublished).
[50] S. M. Sze, *Physics of Semiconductor Devices*. (John Wiley & Sons, Inc., 1981).